Nanoscale

ROYAL SOCIETY OF CHEMISTRY

MINIREVIEW

View Article Online
View Journal | View Issue

Cite this: *Nanoscale*, 2022, **14**, 6743

Halide perovskites and perovskite related materials for particle radiation detection

Fangze Liu, *[a] Rong Wu,[b] Yicheng Zeng,[b] Jing Wei, [b] Hongbo Li, [b] Liberato Manna [c] and Aditya D. Mohite *[d]

Received 6th March 2022,
Accepted 20th April 2022

DOI: 10.1039/d2nr01292h

rsc.li/nanoscale

Radiation detectors are widely used in physics, materials science, chemistry, and biology. Halide perovskites are known for their superior properties including tunable bandgaps and chemical compositions, high defect tolerance, solution-processable synthesis of films and crystals, and high carrier diffusion length. Recently, halide perovskites have attracted enormous interest as particle radiation detectors for both charged (α and β) and uncharged (neutrons) particles. Solid-state detectors based on single crystal perovskites can detect α particles and thermal neutrons with energy-resolved spectra. Halide perovskite scintillators are also able to detect β particles and fast neutrons. In this review, we briefly introduce the fundamentals of radiation detection and summarize the recent progress on halide perovskite detectors for particle radiation.

1. Introduction

The development of modern science and technology relies heavily on advanced experimental techniques. High energy radiation, which can be classified as electromagnetic radiation (X-rays and γ-rays) and particle radiation (α particles, β particles and neutrons), is an important field of research in physics,[1,2] materials science,[3] structural chemistry,[4] and molecular biology.[5] X-rays, γ-rays and neutrons are powerful tools for non-destructive inspection, for example, medical imaging,[6] industrial monitoring,[7] and security inspection.[8] High energy radiation is also extremely relevant in crystallography,[3] nuclear materials,[9] particle physics[1] and astronomy.[2] Therefore, high performance radiation detectors are pivotal to fully extract the information carried by the high energy photons and particles.

All radiation detectors operate under the same principle, that is, converting radiation into electrical or optical signals that can be amplified and processed by conventional electronics. Hence, besides the radiation specific requirements, they need to satisfy a few common requirements, including high absorption cross section, high charge carrier/photon conversion efficiency, high radiation hardness and low background radiation. The detection of radiation relies on partial or complete energy transfer from the photons/particles to the detector material. Therefore, it is important to understand the interactions between radiation and materials, which can be discussed in three groups, namely, electromagnetic radiation (X-rays and γ-rays), charged particles (α and β particles), and uncharged particles (neutrons). The schematic of interactions between different types of radiation and materials is shown in Fig. 1a. However, different types of radiation are not really isolated, as for example a radioactive decay can emit all three types of radiation,[10] and the interaction of a sample with one type of radiation may introduce other types of radiation, *e.g.*, the absorption of high energy X-rays may generate β particles and α particle irradiation can produce X-rays.[11] Therefore, the interaction between high energy photons and materials will also be briefly introduced, although this review will focus only on detectors for particle radiation. Note that only interactions with solid materials will be discussed here, since liquid or gas filled detectors are not related to perovskite materials.

After an X-ray or a γ-ray photon enters the detector, it may interact with the electrons or with the nuclei. Three interactions mainly contribute to the energy transfer from the incident photon to the detector material, *i.e.*, Compton scattering, photoelectric absorption, and pair production.[12] The Compton scattering occurs when the incident photon is scattered by the outer shell electron, and part of the photon energy is transferred to the scattered electron. The photoelectric absorption is the complete absorption of the high energy photon by an inner shell electron, producing a photoelectron with kinetic energy equals to the photon energy minus the binding energy

[a]*Advanced Research Institute of Multidisciplinary Sciences, Beijing Institute of Technology, Beijing, 100081, China. E-mail: fliu@bit.edu.cn*
[b]*Beijing Key Laboratory of Construction Tailorable Advanced Functional Materials and Green Applications, Experimental Center of Advanced Materials, School of Materials Science and Engineering, Beijing Institute of Technology, Beijing 100081, China*
[c]*Nanochemistry Department, Istituto Italiano di Tecnologia, 16163 Genova, Italy*
[d]*Department of Chemical and Biomolecular Engineering, Department of Material Science and Nanoengineering, Rice University, Houston, TX, 77005, USA. E-mail: adm4@rice.edu*

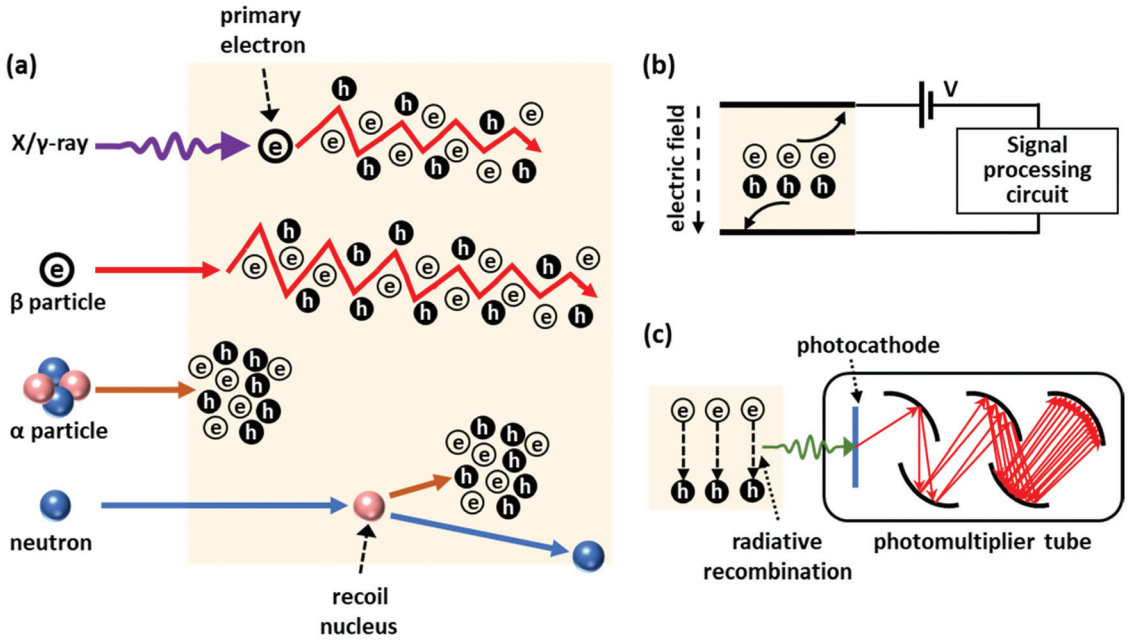

Fig. 1 (a) Sketch of interactions between different types of radiation and materials. Note that only the most important interactions are illustrated. X-rays and γ-rays can transfer all their energy to a primary photoelectron, which converts its energy into many electron–hole pairs. A β particle loses its energy though multiple scattering processes with electrons. An α particle converts its kinetic energy into electron–hole pairs in a short range through may interactions with electrons. A neutron may be scattered by a nucleus, and the recoil nucleus interacts with electrons through Coulomb force. (b) Sketch of a solid-state detector. Electrons and holes are driven by the electric field and collected by the contacts. The signal is further processed by external electronics. (c) Sketch of a scintillator. Electron–hole pairs recombine radiatively and emit visible photons. These photons are detected and amplified into electrical signals by a PMT.

of the electron. The pair production involves the generation of an electron-positron pair after the incident photon is absorbed by the intense coulombic electric field near the nuclei. Thus, it can only take place when the photon energy is larger than the rest energy of the electron-positron pair (1.022 MeV). The secondary electrons, including photoelectrons containing the entire energy of the absorbed photons, the scattered electrons containing a fraction of the energy of the scattered photons, and the electron–positron pairs will undergo a series of elastic and inelastic scattering event and will ultimately convert their kinetic energy into many electron–hole pairs of which the number is calculated by dividing the total energy by the creation energies of electron–hole pairs (E_{pair}, in the range of a few eV).[13,14] The cross sections of all three interactions increase with the atomic number (Z), and thus high Z materials are preferred, especially for detecting high energy X-rays and γ-rays that can penetrate millimeters to centimeters into common detectors.

In the case of charged particles, the interactions are primarily scattering of the electrons in the material atoms through Coulomb force. The energy of the scattered electrons is eventually converted into electron–hole pairs, similar to the case of X-rays and γ-rays. For an α particle, since its mass is much larger than that of an electron, each collision can only transfer a small fraction of its total kinetic energy. However, due to the large cross section, an α particle can interact with many electrons in a short range and lose all its energy. Additionally, a tiny fraction of α particles can also be scattered by the nuclei, a process known as Rutherford scattering, named after Ernest Rutherford.[15] Hence, the penetrating depth of α particles is short. For example, a 10 μm thick gold foil can stop most 1 MeV α particles.[16] The β particles interact in a way similar to that of α particles, except that the penetrating depth (millimeters) is longer than that of α particles due to the lower cross section.[17] Additionally, high energy β particles may lose energy through bremsstrahlung (breaking radiation) and emit high energy photons.[18] Those photons will interact with the detector in the same way as X-rays or γ-rays. For all charged particles, the cross sections also increase with Z, but low Z materials can also be used in detectors since the penetrating capability of charged particles is not as strong as that of high energy photons.

The detection of neutrons is more difficult than that of charged particles because they cannot interact with materials through Coulomb force. Therefore, the detection depends primarily on elastic scattering with the nuclei, and the cross sections are small for most materials. The only exception is represented by thermal neutrons (energy less than 1 eV), which can be efficiently captured by a few specific nuclei, *i.e.*, ^{3}He, ^{10}B, ^{6}Li and ^{157}Gd through nuclear reactions. Such reactions produce secondary emissions including protons, α and β particles, and electromagnetic radiation.[19] For fast neutrons, since elastic scattering dominates the interaction, hydrogen becomes the most effective absorber because its nucleus has

the same mass as the neutron. The recoil nucleus (proton for hydrogen) behaves similarly to an α particle and transfers its energy to the surrounding electrons.

Radiation detectors can be classified as direct-conversion (solid-state) detectors (Fig. 1b) and indirect-conversion detectors (scintillators, Fig. 1c) by their working mechanisms.[20] A solid-state detector directly collects the electron–hole pairs generated by the incident photons/particles by applying an electric field across the detector. To facilitate the charge transport and maximize the charge collection efficiency, the detector materials need to have mobility–lifetime products ($\mu\tau$ products) that are large enough for the electrons or holes to travel through the detector and arrive at the contacts. Moreover, to minimize the leakage current under a large electric field, the bandgaps of detector materials must be relatively large, and the defect densities must be small. Thus, solid-state detectors often utilize semiconductors that can be grown into large crystals with low defect density. The scintillators convert the radiation into visible light through radiative recombinations of the electron–hole pairs, and these visible photons are further detected by a charge-coupled device (CCDs), complementary metal–oxide semiconductor (CMOS), photomultiplier (PMT) or silicon photomultiplier (SiPM).[13,14] A good scintillator needs to meet the following requirements: high light yield, which is defined by the number of emitted photons per absorbed radiation energy (MeV), fast emission, which is important for time sensitive detection, and proper emission wavelength to maximize the efficiency of the coupled optical detector.

The detectors can also be categorized by their working mode, for example, integrating mode and single photon/particle counting mode (spectrometer). The integrating mode integrates all signals (electrical charges from solid-state detectors or visible photons from scintillators), and the output is equal to the total energy that the radiation deposits to the detector during the exposure. The integrating mode is usually used in imaging detectors, for example, X-ray medical imaging[6] and neutron imaging,[21] where the image contains only contrast information, indicating the different absorptions from different materials.[22] The performance of integrating detectors is thus measured by the sensitivity, defined by the charges/photons per unit dose.[22] The single photon/particle counting mode counts each high energy photon/particle individually, and the output signals are often processed by charge sensitive amplifiers and converted into voltage pulses of which the heights are proportional to the energy deposited by the incident photon/particle. Thus, the energy spectrum of the radiation can be extracted by plotting the histogram of the pulse height after proper energy calibration.[23] The critical performance of single photon/particle counting detectors is measured by their energy resolution, calculated by the full width at half maximum (FWHM) of the energy peak divided by the center energy.[24] This is particularly important for γ-ray and charged particle detectors for isotope identification,[25] single photon-emission computed tomography (SPECT),[26] energy-resolved X-ray imaging[27] and neutron spectroscopy.[28]

Notably, PMTs in combination with scintillators are primarily used as single photon/particle counting detectors.[29,30] PMTs are also widely used as photodetectors for spectroscopy and biological fluorescence detection.[31,32] The basic working principle of a PMT is the transformation, by means of a photocathode, of incident photons into photoelectrons, which are extensively amplified through a series of secondary electron emissions inside the PMT. Therefore, the photocathode is the crucial component in determining the efficiency and spectral range of a PMT.

Halide perovskites are a group of materials that share the same crystal structure as the mineral perovskite.[33] The three-dimensional (3D) perovskites have a general chemical formula of ABX_3, where A is an organic or inorganic cation (MA^+: methylammonium, FA^+: formamidinium, Cs^+, Rb^+, *etc.*), B is an metal cation (Pb, Sn, Bi, *etc.*), and X is a halide anion (Cl, Br, I). Since the initial exciting works on 3D halide perovskites,[34] other perovskite-related materials have also been widely studied, including the so-called two-dimensional (2D) perovskites,[35] zero-dimensional (0D) perovskites,[36] double perovskites[37] and many other perovskite-like materials.[38] In this review, we will use the term "halide perovskites" when referring to both perovskite and perovskite-related materials.

Halide perovskites have received enormous attention during the last decade, mainly for their strong potential to achieve low-cost solar cells.[39–41] Thanks to their superior properties, *i.e.*, tunable bandgaps and chemical compositions, high defect tolerance, solution-processable synthesis of films and crystals, and high carrier diffusion length, halide perovskites have also been exploited in prototype light-emitting diodes,[42–45] lasers,[46] optical detectors,[47] field-effect transistors,[48,49] and photocatalysts.[50] Also, radiation detectors based on halide perovskites have attracted considerable interest during the past few years, especially for electromagnetic radiation detectors.

Halide perovskites are known as effective absorbers for high energy photons, primarily due to the heavy atoms including Pb, Cs and I. They also meet all necessary requirements for both solid-state detectors and scintillators. In terms of solid-state detectors, halide perovskites have high $\mu\tau$ products that can facilitate charge carrier transport. They also have suitable bandgaps that can give low leakage current for low detection limit. Polycrystalline thin films are often used for X-ray detectors, while single crystals are usually required to ensure the complete absorption of high energy γ photons. In the case of scintillators, halide perovskites possess high radioluminescence quantum yield for efficient detection of high energy photons. The emission wavelength of halide perovskites is also tunable within the visible and near infrared range, which can match the maximum detection efficiency of the coupled photodetectors. Therefore, perovskite scintillators based on both single crystals and nanocrystals have succeeded in detecting X- and γ-rays.

Perovskite X-ray detectors, both solid-state detectors and scintillators, have shown superior sensitivity compared with conventional materials.[51–55] The energy resolution of perovs-

kite γ-ray detectors has been improving rapidly, and detectors based on inorganic perovskite $CsPbBr_3$ have demonstrated performances comparable to those of established CdZnTe ternary alloys.[56–59] A few comprehensive review articles published lately have summarized these recent progress on electromagnetic radiation detectors based on halide perovskite, for example, X-ray detectors,[51,60] γ-ray detectors,[59] and both.[61,62] Recently, significant efforts have been made toward particle radiation detection using halide perovskites, for example for detecting α particles,[63–65] β particles,[66] thermal neutrons,[67,68] and fast neutrons.[69,70] Therefore, this review will aim at summarizing the current status on particle radiation detectors based on halide perovskite. The recently reported photocathodes using halide perovskites will also be included. Finally, we will also provide an outlook on these fields.

2. Halide perovskites for α particle detector

An α particle consists of two protons and two neutrons and is categorized as a heavily charged particle. The α particles can be generated by many radioactive isotopes (radium, uranium, americium, plutonium, *etc.*), and thus represent a characteristic radiation in the identification of these isotopes.[73] α particles strongly interact with electrons in the detector material. Although each scattered electron can only take a small fraction of the total kinetic energy of an α particle, many electrons can interact with the α particle in a short distance and completely stop it. The penetrating depth of α particles, centimeters in air and micrometers in solid, is the shortest among all types of radiation considered in this review.[16] Therefore, the air gap between the source and the detector must be taken into consideration. Owing to the short penetrating depth, high Z materials are not required for α particle detection, and low Z semiconductors with high $\mu\tau$ products can make good solid-state detectors. The state-of-the-art diamond detectors can resolve the 5.486 MeV α particles from an ^{241}Am radioactive source with an energy resolution of 0.3%.[74,75] Scintillators can also discriminate the energy spectra from α particles effectively. ZnSe scintillators doped with Te can produce the spectrum of ^{239}Am α particles with highest energy resolution of 3% at 5.15 MeV.[76,77] There are several reports on halide perovskites for α particle detection, including 3D perovskite $MAPbBr_3$, $MAPbI_3$ and $CsPbBr_3$,[63,71,78] 2D perovskite $(BA)_2PbBr_4$ (BA: butylammonium) and $(BDA)CsPb_2Br_7$ (BDA: 1,4-butanediamine),[65,79] 0D perovskite Cs_4PbBr_6 and Cs_4PbI_6,[72,80] and other perovskite related structures ($Cs_3Bi_2I_9$, Cs_2TiI_6, Cs_2CrI_6, *etc.*).[64,81,82]

2.1 Solid state detectors for α particle

Solid state α particle detectors have been demonstrated by using 3D, 2D and defect perovskites. The material properties and detector performance are summarized in Table 1. An early attempt to detect α particles using solid-state detectors based on halide perovskites was reported by Xu *et al.*[63] A single crystal $MAPbBr_3$ grown by anti-solvent solution process was deposited by Cr and C_{60}/bathocuproine (BCP)/Cr contacts as cathode and anode, respectively. Although energy spectra could be acquired from the detector under an ^{241}Am α source, the spectral peaks were broad, and the peak position did not scale linearly with the applied voltage. This was attributed to the high dark current level (206 ± 10 nA cm^{-2}) and the unbalanced electron and hole transport. Detectors based on $MAPbI_3$ single crystals reported by He *et al.* presented better performance in detecting ^{241}Am α particles.[71] The $MAPbI_3$ detector exhibited a lower dark current of ~81 nA cm^{-2} and a more balanced electron and hole transport. Consequently, it could detect the 5.5 MeV ^{241}Am α particles with an energy resolution of 14%. (Fig. 2a and b) The same group also reported detectors using inorganic $CsPbBr_3$ single crystals.[78] The detector, with a structure of In/$CsPbBr_3$/Au, can simultaneously resolve the γ-ray (122 keV)and α particle (5.5 MeV) peaks from a ^{57}Co source with energy resolutions of 4.8% and 15%, respectively. Compared with organic–inorganic perovskites, inorganic perovskites possess higher stability and lower defect density when they are grown by the Bridgman method,[83] and have great potential in competing with the current technology for α particle detection, especially considering the recent progress on high-resolution γ-ray detectors based on $CsPbBr_3$.[57]

2D perovskites have a quantum well structure, with layers of lead halide octahedra separated by layers of organic molecules.[84,85] They have higher stability and larger exciton binding energy than 3D perovskites, thus they are promising for optoelectronics.[86] Xiao *et al.* tested solid-state detectors using 2D Dion-Jacobson perovskite $(BDA)CsPb_2Br_7$ single crystals.[65] (Fig. 2c and d) The 2D perovskite had a large band gap of 2.76 eV and a high resistivity of 4.35×10^{10} Ω cm. The detector had a low dark current density of 34 nA cm^{-2}, and the

Table 1 Performance of α particle solid-state detectors

Material	Growth method	Structure	$\mu\tau$ product (cm^2 V^{-1})	Charge collection efficiency (%)	α source	Energy resolution (%)	Ref.
Diamond	CVD	Al/diamond/TiC/Au	3.1×10^{-4} (h)	100	5.5 MeV ^{241}Am	0.3%	75
$MAPbBr_3$ SC	Solution	Cr/$MAPbBr_3$/C_{60}/BCP/Cr	$(0.4–1.6) \times 10^{-3}$ (h)	—	5.5 MeV ^{241}Am	—	63
$MAPbI_3$ SC	Solution	Pb/$MAPbI_3$/Au	8.1×10^{-4} (h)	—	5.5 MeV ^{241}Am	14%	71
$CsPbBr_3$ SC	Bridgman	In/$CsPbBr_3$/Au	9.5×10^{-4} (h)	—	5.5 MeV ^{241}Am	15%	78
$Cs_3Bi_2I_9$	Bridgman	Au/$Cs_3Bi_2I_9$/Au	5.4×10^{-5} (e)	—	5.5 MeV ^{241}Am	—	64
$CsPbBr_{2.4}Cl_{0.6}$	Solution	Ga/$CsPbBr_{2.4}Cl_{0.6}$/Au	3.26×10^{-4} (h)	—	5.5 MeV ^{241}Am	42%	92

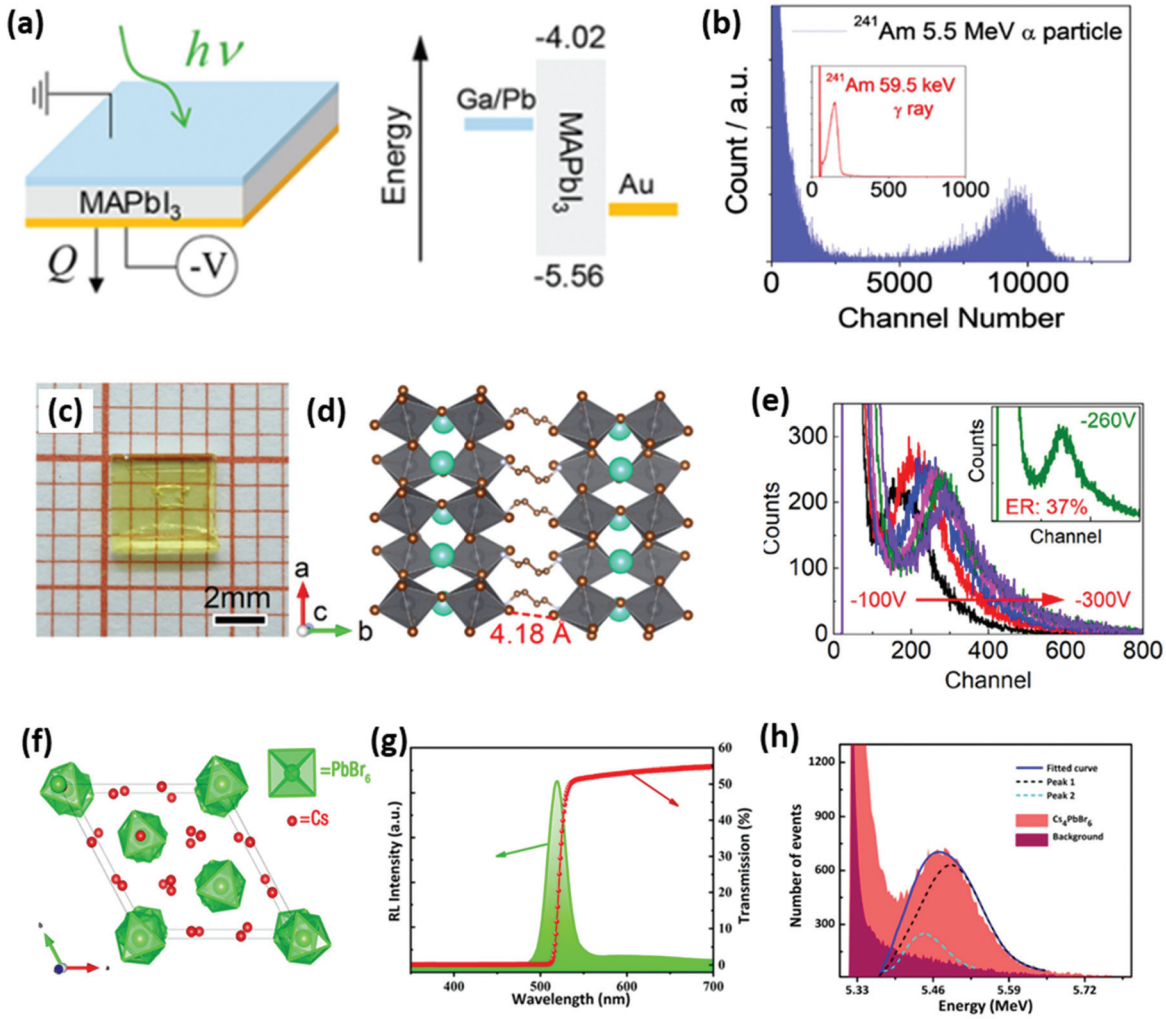

Fig. 2 (a) Sketch of the $MAPbI_3$ detector (left) with asymmetric contacts and the corresponding band diagram (right). (b) Energy spectrum acquired by a $MAPbI_3$ detector at room temperature under ^{241}Am radiation source with both α particles (5.5 MeV) and X-rays (59.5 keV). The inset is the low energy section of the energy spectrum corresponding to the 59.5 keV X-ray peak. Reproduced with permission from ref. 71. (c) Photograph of a $(BDA)CsPb_2Br_7$ single crystal. Copyright 2018 American Chemical Society. (d) Sketch of the crystal structure of $(BDA)CsPb_2Br_7$. (e) The energy spectra of a $(BDA)CsPb_2Br_7$ detector under an ^{241}Am source. Reproduced with permission from ref. 65. Copyright 2022 American Chemical Society. (f) Sketch of the Cs_4PbBr_6 crystal structure. (g) Radioluminescence and transmission spectra of a Cs_4PbBr_6 crystal. (h) Pulse height spectrum of a Cs_4PbBr_6 single crystal scintillator under an ^{241}AM source. Dashed lines are Gaussian peak fit. Reproduced with permission from ref. 72. Published 2021. Licensed under CC BY 4.0.

energy resolution for ^{241}Am α particles was 37% (Fig. 2e). While the energy resolution still falls behind those of 3D perovskite, 2D perovskites hold great promise as α particle detectors.

Other perovskite related structures have also been explored as radiation detectors. For example, solid-state detectors made of defect perovskites in the form of $A_3M_2I_9$ ($Rb_3Bi_2I_9$, $Rb_3Sb_2I_9$, $Cs_3Bi_2I_9$ and $Cs_3Sb_2I_9$) were able to detect α particles.[64] However, no energy-resolved spectrum was acquired. Although the perovskite-based detectors have shown their performance for efficient α particle detection, their performance still fall largely behind that of the established diamond detector,[75] especially for the energy resolution. In addition, the charge collection efficiency (CCE), defined by the amount of collected charge relative to the generated charge inside the detector by radiation, is also an important performance indicator for solid-state detectors. A high CCE usually indicates that the detector is free of charge traps. Although no perovskite detector has reported CCE values, it is reasonable to assume that their CCEs are much lower than that of the diamond detector (100%), which is also related to their difference performance in the energy resolution. Compared with scintillators, solid-state α particle detectors are more compact and can provide high energy resolution. But the requirement for good carrier transport capabilities also limits the material selections. Future studies need to focus on improving the crystal quality of halide perovskites and optimizing the device structure to improve both CCE and energy resolution.

Table 2 Performance of α particle scintillators

Material	Growth method	Wavelength (nm)	Light yield (ph MeV^{-1})	Decay time	α particle	Energy resolution (%)	Ref.
ZnSe(Te)	Bridgman	640	70 000	30–80 μs	5.15 MeV ^{239}Pu	3	76 and 77
$(BA)_2PbBr_4$ microcrystals	Solution	427	7000	1.70 ns	^{237}Np	24.29	79
Cs_4PbBr_6 SC	Solution	525	—	1.46 ns	5.5 MeV ^{241}Am	58.7	72
Cs_4PbI_6 SC	Solution	552	—	0.95 ns	4.78 MeV ^{237}Np	35	80
					5.15 MeV ^{239}Pu	36	
					5.5 MeV ^{241}Am	43	

2.2 Scintillators for α particle

Scintillators for α particles were built with 2D and 0D perovskites. The material properties and scintillator performance are summarized in Table 2. Li *et al.* synthesized $(BA)_2PbBr_4$ microcrystals for α particle scintillation.[79] The material emitted at 427 nm with a moderate light yield of 7000 ph MeV^{-1}, comparable to that of a commercial plastic scintillator EJ228 (10 200 ph MeV^{-1}) under the same conditions. The energy resolution for α particles from a ^{237}Np source was about 24%. In the 0D Cs_4PbBr_6 structure, the lead halide octahedra are disconnected and separated by Cs^+ cations (Fig. 2f). A green emission from this material has been observed by many groups and attributed to a multitude of possible causes, including the likely presence of $CsPbBr_3$ impurities.[87–90] Li *et al.* demonstrated scintillators using Cs_4PbBr_6 single crystals with a high PLQY of 86.7% at 525 nm.[72] However, the energy resolution for 5.5 MeV α particles was only 58.7%, probably due to the poor photon collection efficiency of the PMT coupled to the scintillator (Fig. 2g and h). The same group further developed Cs_4PbI_6 single crystal scintillators and achieved improved energy resolution of 43% for 5.5 MeV α particles.[80] The light yield of the Cs_4PbI_6 scintillator was about 50% of that from a commercial BGO scintillator. Since its absolute light yield was not reported, the improved energy resolution may originate from the increased light yield or the improved photon collection efficiency of the PMT.

These early demonstrations again emphasize the potential of using halide perovskite scintillators for α particle detection. However, their relative low light yield seriously limits the performance of perovskite scintillators. Since only a few halide perovskites have been tested for α particle scintillators, much less than the case of X-ray scintillators,[51] more halide perovskites can be tested to search for the best performing scintillators, especially for perovskite nanocrystals which are so far the most promising X-ray scintillators based on halide perovskite.[91]

3. Halide perovskites for β particle detector

β particles are high energy electrons or positrons emitted by certain nuclides. Detecting β particle is important for radioactive contamination surveillance.[93] They have moderate penetration ability, that is, higher than α particles but lower than X-rays. β particles can undergo elastic or inelastic scattering after entering the absorbing materials, and the inelastically scattered electrons can further generate secondary emissions (Auger electrons, secondary electrons, and X-rays). This secondary radiation is ultimately converted into electron–hole pairs and contributes to the detector signal. The elastic scattering between the β particles and the nuclei may result in backscattering, where the fast electrons are deflected by a large-angle and escape the detector, depositing little energy to the detector. The probability of backscattering increases with Z and is more prominent for low energy electrons, *i.e.*, a thick gold layer can reflect 50% of incoming 100 keV electrons while carbon can only reflect 4%.[94] Therefore, low-Z elements are more favourable for β particle detectors. Using light elements can also lower the detector sensitivity to X- and γ-rays, resulting in higher discrimination of the β signal.

Halide perovskites have only been demonstrated as scintillators for β particle until now, summarized in Table 3. The first halide perovskite β scintillator was reported by Yu *et al.*[66] They selected 2D perovskites for their lower average Z values compared with 3D perovskites and higher irradiation hardness.[95] A reference scintillator based on $CsPbBr_3/Cs_4PbBr_6$ perovskite core/shell nanocrystals (NCs) was also tested. The difference of electron backscattering can be seen from the SEM image of the sample containing both 2D perovskite and high Z perovskite NCs (Fig. 3a), where the 2D perovskite had lower electron backscattering (brightness). To improve the PLQY and reduce reabsorption, Mn dopants (~0.3%) were introduced to increase the Stokes shift, and the PLQY was raised from less than 10% for undoped perovskites to over 50% for Mn doped ones. The highest β scintillation light yield (24 000 ph MeV^{-1}) was achieved from the long-chain STA_2PbBr_4 (Fig. 3b–d). The 2D perovskite scintillator also displayed good linearity as well as high β irradiation hardness. (Fig. 3e and f).

Besides pure perovskite crystals, halide perovskites embedded in plastic scintillators were also found to be effective β scintillators.[96] Kang *et al.* synthesized an epoxy/PPO/perovskite (PPO: 2,5-diphenyloxazole) composite by simply mixing 0.5 wt% $CsPbBr_{3-x}Cl_x$ with epoxy/PPO mixture. After annealing the mixture at 250 °C, the perovskite formed nanoparticles, and the scintillator remained highly transparent (Fig. 3g). Also, the epoxy–PPO/perovskite scintillator featured a large Stokes shift, significantly reducing reabsorption (Fig. 3h). Under β irradiation from a ^{90}Sr source, the perovskite

Table 3 Performance of β particle detectors

Material	Growth method	Wavelength (nm)	Light yield (ph MeV^{-1})	Decay time (ns)	β source	Energy resolution	Ref.
STA_2PbBr_4:Mn	Aqueous synthesis	610	24 000	500	^{63}Ni (up to 66.7 keV)	—	66
Epoxy/PPO/$CsPbBr_{3-x}Cl_x$	Thermal polymerization	430	—	—	^{90}Sr (up to 546 keV)	—	96

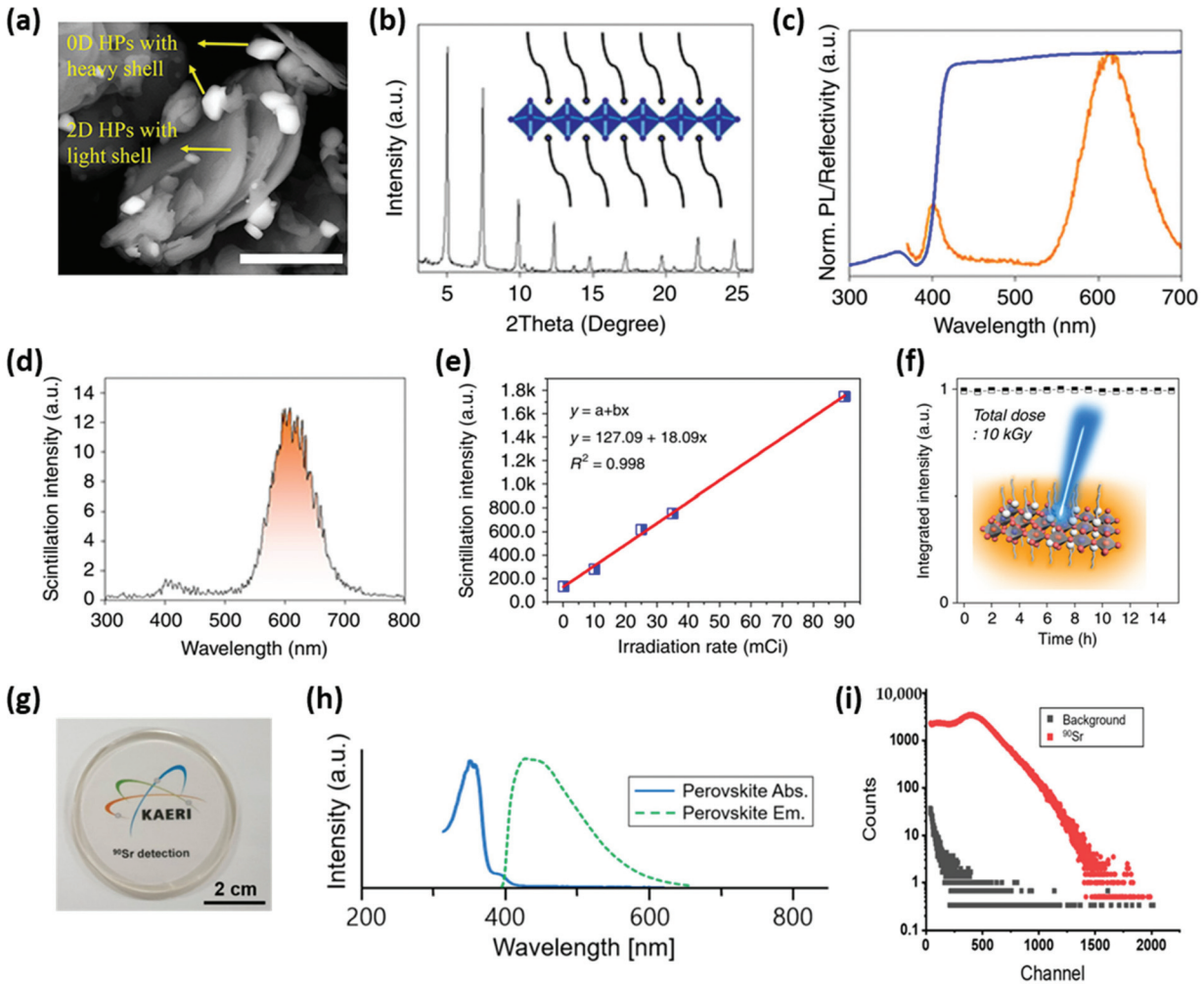

Fig. 3 (a) SEM image of the mixture of perovskite NCs ($CsPbBr_3/Cs_4PbBr_6$) and 2D perovskites (STA_2PbBr_4) in backscattering electron mode indicated the different electron reflectivity, the scale bar is 5 μm. Note that the 0D HPs in the image represented perovskite NCs. (b) XRD of STA_2PbBr_4 with the inset showing the sketch of the lattice structure. (c) Scintillation spectrum of STA_2PbBr_4. The 2D perovskite scintillator demonstrated I good linearity down to the detection limit and (f) high β irradiation hardness. Panels (a–f) are reproduced with permission from ref. 66. Published 2020. Licensed under CC BY 4.0. (g) A photograph of epoxy matrix with PPO and a perovskite-loaded plastic scintillator. (h) Absorption and emission spectra of the perovskite-loaded scintillator. (i) Energy spectrum acquired from the perovskite-loaded plastic scintillator. Panels (g–i) are reproduced with permission from ref. 96. Published 2021. Licensed under CC BY 4.0.

scintillator could generate an energy spectrum with higher counts in the high energy range (channel number higher than 800) than the commercial scintillator BC-400 (Fig. 3i). It also proved a neutron detection efficiency of 17.71%, close to that of BC-400 (20.05%), demonstrating the potential applicability of halide perovskites in plastic scintillators.

Although the reported β particle scintillators based on halide perovskite have high light yield comparable to commercial plastic scintillators, they failed to resolve the energy of β particles. Since the first report of β particle detectors based on halide perovskites was only two years ago, many questions remain open and need comprehensive studies. Noting the similarities between X-/γ-ray detectors and β particle detectors, future studies may adopt similar selections of materials and device structures of the former for the latter, for both solid-state detectors and scintillators, which will also allow the

direct comparison between these two types of detectors. To address the issue of electron backscattering caused by heavy atoms, perovskites consisting light elements instead of lead may be considered, for example, Sn and Cu based perovskites.

4. Halide perovskites for neutron detector

Neutron detectors are widely used for a variety of applications, for example neutron crystallography,[97] nuclear reactor instrumentation,[98] nuclear material detection,[99] and nuclear physics.[100,101] Unlike γ-rays or charged particles, neutrons interact weakly with electrons. Therefore, the detection of neutrons relies on their interaction with nuclei, releasing charged particles that can be converted into electrical signals. Neutrons can be classified according to their energy range, from low to high energy, cold neutrons (<25 meV), thermal neutrons (~25 meV), epithermal neutrons (25 meV to 100 eV), slow neutrons (100 eV to 1 MeV), and fast neutrons (>1 MeV).[102] Only a few nuclei can efficiently capture thermal neutrons, for example, ^{3}He, ^{10}B, ^{6}Li and ^{157}Gd.[19] Therefore, thermal neutron detectors must use materials with a high density of these nuclei. On the other hand, because fast neutrons interact weakly with most nuclei, the most effective detection is through elastic scattering with hydrogen nuclei (protons), and the fast neutron detectors often contain hydrogen-rich plastics.[103] In addition to high interaction probability, neutron detectors also need to meet two requirements: low γ-ray sensitivity and high α particle detection efficiency.[104] Since the generation of neutrons is often accompanied by the emission of γ-rays, it is important not to count the false neutron events from γ-ray absorption. This can be done by either using a material containing only light elements that have low γ-ray absorption coefficient or using pulse shape discrimination (PSD) enabled by the different time scale between a neutron pulse and a γ pulse.[105]

Since α particle is the characteristic product after a neutron being captured by a ^{10}B or ^{6}Li nucleus, measuring α particle with high efficiency and high energy solution is essential for precise neutron count. ^{3}He gas has been the most widely material used in gas proportional detectors by producing a ^{1}H and a ^{3}H ions after absorbing a thermal neutron. However, due to the very limited production of ^{3}He gas along with the bulky volume, high operation voltage and high cost of gas proportional detectors, these cannot meet the increasing demand for more affordable and portable detectors.[107] Scintillators and solid-state detectors are therefore highly sought for affordable, compact and pixelated neutron detection.[104,108,109]

Neutron scintillators often use glass or semiconductors containing ^{6}Li, for example, ^{6}Li-glass, ^{6}LiI and ^{6}LiF/ZnS.[108] ^{10}B and ^{6}LiF filled Si microstructures have been the most successful solid state neutron detectors with high detection efficiencies over 30%.[110,111] These detectors are considered as indirect-conversion solid-state detectors because the neutron absorption and charge collection are separated in different materials. The thermal neutrons are first captured by the ^{10}B and ^{6}LiF coatings, which release energetic charge particles (^{3}H and α from ^{6}Li, ^{7}Li and α from ^{10}B). Only those charged particles reaching the Si diode can create electron–hole pairs that are converted to electrical signals.[104] Therefore, the detection efficiencies of indirect-conversion detectors are lower than those of direct-conversion detectors that use one material for both neutron capture and charge collection. Popular materials for direct-conversion neutron detectors are hexagonal boron nitride (hBN),[112] $LiInSe_2$[113] and $LiInS_2Se_6$.[114] These materials can potentially offer 100% detection efficiency as well as high energy resolution. In spite of such recent progress on direct-conversion neutron detectors, many issues remain unsolved, for example, the growth of high-quality crystals and the detector optimization. Therefore, new materials for neutron detection, especially direct-conversion detectors are still under active investigation. Several reports have demonstrated neutron detectors based on halide perovskites, including both scintillators and indirect-conversion solid-state detectors.[67–70,106,115,116] Since the detectors for thermal and fast neutrons require different absorbing materials, they will be discussed separately below.

4.1 Thermal neutron detectors

4.1.1 Solid-state detectors for thermal neutrons. Both 3D inorganic and organic–inorganic halide perovskites have been shown as thermal neutron detectors, summarized in Table 4. An indirect-conversion solid-state thermal neutron detector was reported by Fernandez-Izquierdo *et al.* using $CsPbBr_3$ thin films combined with a ^{10}B conversion film.[67] The diode used a structure of ITO/Ga_2O_3/$CsPbBr_3$/Au where the Ga_2O_3 was the n-type contact. The diode exhibited reasonable α particle response, which was 16% of that of a commercial Si diode. The neutron detection was achieved by placing a commercial ^{10}B conversion layer on top of the Au contact, and the neutron detection was calculated as ~1% for the $CsPbBr_3$ diode. This efficiency could be further improved by doping the surface of $CsPbBr_3$ with Cl anion coming from the treatment with $PbCl_2$ vapor. Compared with undoped $CsPbBr_3$ film, the mixed halide film was characterized by larger grains and lower leakage current, and consequently the neutron detection efficiency increased to 2.5%, fairly close to that of a reference Si diode. The indirect-conversion detectors based on $CsPbBr_3$ were further improved by the same group recently.[106] The ^{10}B conversion layer was backfilled into the microstructures etched on the $CsPbBr_3$ film, similar to the ^{10}B filled Si microstructures.[110] (Fig. 4a) The ^{10}B filled $CsPbBr_3$ detectors had a maximum neutron detection efficiency of 4.3%, much improved than that of planar detectors.[67] (Fig. 4b) In general, thin film detectors are insensitive to γ-rays owing to their micrometer thickness (13 μm), thus a high neutron-γ discrimination was achieved for precise neutron count.

Organic–inorganic halide perovskite were also demonstrated as indirect-conversion thermal neutron detectors. Bouanani *et al.* used polished $MAPbBr_3$ single crystals (thickness of 100 μm) in a diode structure of Ag/In/Ga_2O_3/$MAPbBr_3$/

Table 4 Performance of solid-state neutron detectors

Material	Growth method	Detector structure	Detection mechanism	Neutron source	Detection efficiency	Ref.
$CsPbBr_3$ film	Close space sublimation	$ITO/Ga_2O_3/CsPbBr_3/Au$	Indirect	^{252}Cf	2.5%	67
$CsPbBr_3$ film	Close space sublimation	$ITO/Ga_2O_3/CsPbBr_3/Au$	Indirect	^{252}Cf	4.3%	106
$MAPbBr_3$ SC	Solution	$Ag/In/Ga_2O_3/MAPbBr_3/Au$	Indirect	^{252}Cf	3.92%	116

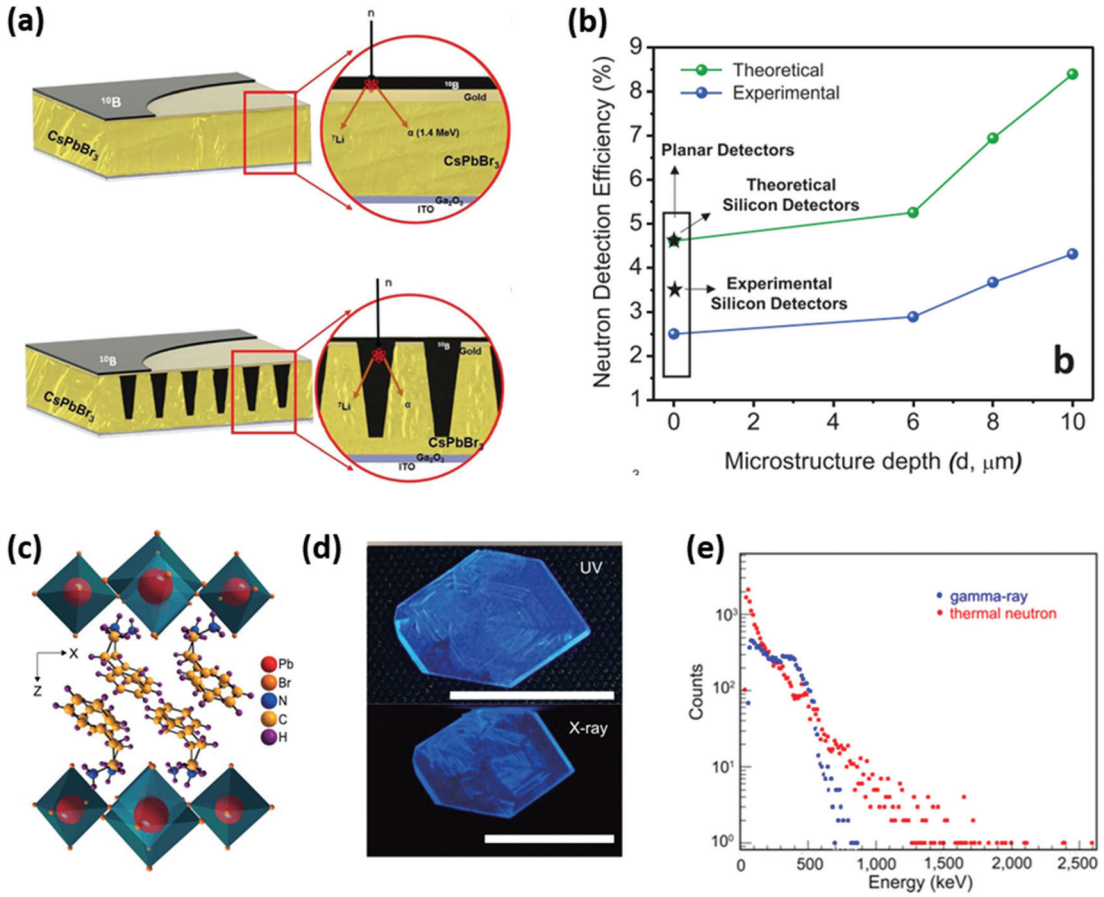

Fig. 4 (a) Sketch of a planar $CsPbBr_3$ neutron detector (top) and a microstructured $CsPbBr_3$ detector back-filled with ^{10}B. (b) Comparison of neutron detection efficiencies between theoretical simulations and experimental results from planar and microstructured $CsPbBr_3$ detectors. The ^{10}B filled detectors showed much improved detection efficiencies. Reproduced with permission from ref. 106. Copyright 2022 Wiley. (c) Sketch of the crystal structure of $(PEA)_2PbBr_4$. (d) Photographs showing UV and X-ray luminescence of a Li–$(PEA)_2PbBr_4$ single crystal. Scale bars are 1 cm. (e) Pulse height spectra from a Li–$(PEA)_2PbBr_4$ scintillator under an Am–Be neutron source after PSD. The neutron and γ-ray (^{137}Cs) spectra are in red and blue dots, respectively. Reproduced with permission from ref. 68. Published 2020. Licensed under CC BY 4.0.

Au for thermal neutron detection.[116] The diodes exhibited low leakage current and high α particle detection efficiency of 59.3%. The neutron detection was achieved by placing a ^{10}B converter on top of the Ag contact, and the neutron detection efficiency reached 3.92%, higher than the planer detector and very closed to the micro-structured $CsPbBr_3$ detectors.[67,106] This improved detection efficiency can be attributed to the thicker film used in this study (100 μm *vs.* 13 μm). However, thick halide perovskite film also increased γ-ray sensitivity and decreased neutron-γ discrimination. Therefore, it is important to find the optimized device thickness for balanced neutron detection efficiency and γ-ray sensitivity. Indirect-conversion detectors based on $MAPbBr_3$ were also reported by Andričević *et al.*[115] The detectors employed a simple device structure of $MAPbBr_3$ single crystals with graphite spray electrodes. A Gd foil or a Gd_2O_3 pellet was used for neutron conversion. Unlike ^6Li or ^{10}B, which releases mainly α particles, Gd converts thermal neutrons main into γ-rays.[117] Hence, the $MAPbBr_3$ detectors were actually for γ-ray detection. Although they showed photocurrent response to the γ-rays emitted by the Gd converter, the discrimination between neutron and γ-ray needs to be further evaluated.

Although these indirect-conversion solid-state detectors can detect thermal neutrons, they are not much different from the

Table 5 Performance of neutron scintillators

Material	Growth method	Wavelength (nm)	Relative light yield compared with reference	Decay time (ns)	Neutron source	Spatial resolution, lp mm^{-1}	Ref.
Li-$(PEA)_2PbBr_4$ SC	Solution	436	—	11 ns	Am–Be thermal neutron	—	68
$FAPbBr_3$ NC	Solution	523	19.3% of ZnS:Cu(PP)	Seconds	1.8 MeV average	0.2	118
$CsPbBrCl_2$:Mn NC	Solution	606	11.24% of ZnS:Cu(PP)	Seconds	>1 MeV	0.37	69
Mn-STA_2PbBr_4 microplates	Solution	620	79% of ZnS:Ag(PP)	812 μs	2 MeV, 14 MeV	0.5	70

α particle detectors introduced in Section 2. Therefore, similar strategies also apply to the further development of indirect-conversion neutron detectors. More importantly, direct-conversion solid detectors that use halide perovskites incorporating neutron-capturing nuclei can offer much higher detection efficiency, and thus the successful synthesis of halide perovskite with high concentration of ^{10}B or ^{6}Li may open new routes for solid-state thermal neutron detector. Since efficient capture of thermal neutrons only requires sub-millimetre thick absorbing material, solid-state detectors can achieve more compact design compared with scintillators, and therefore more favourable for thermal neutron detection.

4.1.2 Scintillators for thermal neutrons. Thermal neutron scintillators were reported by Xie *et al.* using 2D halide perovskite crystals.[68] The material properties and scintillator performances for both thermal and fast neutrons are summarized in Table 5. Li doped layered perovskite $(PEA)_2PbBr_4$ (Li–$(PEA)_2PbBr_4$) single crystals were synthesized by adding LiBr to the $PbBr_2$ precursor, and the highest Li : Pb ratio was 1 : 20. The Li–$(PEA)_2PbBr_4$ single crystal was found to be a good scintillator for X-ray, γ-ray and α particles. (Fig. 4c and d) Additionally, the incorporation of Li enabled thermal neutron capture, although the detection efficiency was low due to the low ^{6}Li concentration in natural Li (7.59%). A clear bump caused by neutron interaction can be discriminated from that caused by γ-rays in the pulse height histograms. (Fig. 4e) These results emphasize the possibility of high-performance thermal-neutron scintillators based on halide perovskite, providing that high concentration ^{6}Li can be applied to the synthesis. Similar to solid-state detectors, halide perovskite consisting high densities of ^{10}B or ^{6}Li that are directly incorporated into the perovskite lattice instead of doping may offer higher scintillation efficiency.

4.2 Fast neutron detectors

Fast neutron scintillators have been demonstrated using perovskite NCs and 2D halide perovskites, which contain high densities of hydrogen atoms, summarized in Table 5.[69,70,118] To maximize the light output, the scintillators need to contain high density perovskite NCs while keeping reabsorption low. Moreover, since the fast neutron scintillators are often used for radiography imaging, high spatial resolution is also an important parameter for evaluating their performance. The first fast neutron scintillator based on perovskite NCs was reported by McCall *et al.* using $FAPbBr_3$ and $CsPbBrCl_2$:Mn NCs.[118] The $FAPbBr_3$ NCs exhibited the highest light yield (19% of the reference ZnS:Cu scintillator) owning to their near unity PLQY (96%) (Fig. 5a and b). Higher concentrations of NCs can increase the charge collection efficiency, however, the light yield did not increase linearly with the concentration, primarily due to the strong reabsorption (Fig. 5c) of $FAPbBr_3$ NCs. The strong reabsorption also increased light scattering, resulting in low spatial resolution. In contrast, the $CsPbBrCl_2$:Mn NCs exhibited almost twice as much spatial resolution as that of $FAPbBr_3$ NCs (27 pixels *vs.* 52 pixels) because of the large Stokes shift, though the PQLY was low due to the low concentration. To further increase the concentration of $CsPbBrCl_2$:Mn NCs and fully utilize their Stokes shift, Montanarella *et al.* improved the synthesis of NCs using a long-chain zwitterionic ligand to attain very high concentrations (over 100 mg ml^{-1}).[69] As a result, the concentrated $CsPbBrCl_2$:Mn NCs maintained both high PLQY (53%) and dominant Mn^{2+} emission (97% of total emission) with 1 eV Stokes shift (Fig. 5d). The light yield of fast neutron scintillation scaled almost linearly with concentration, close to that of $FAPbBr_3$ NCs whose PLQY was almost twice (96% *vs.* 53%). (Fig. 5e) Overall, NCs hold great promise for fast neutron scintillation, and the ideal material needs to simultaneously satisfy high PLQY, large Stokes shift and high concentration.[53,91]

Beside perovskite NCs, 2D halide perovskite Mn-$(C_{18}H_{37}NH_3)_2PbBr_4$ (Mn-STA_2PbBr_4) microplates were also tested as fast neutron scintillator by Zheng *et al.*[70] The hydrogen density was enriched by the long chain stearylamine (STA) cation. (Fig. 5f) Therefore, both neutron scattering and luminescence generation were integrated into a single perovskite compound. Since the undoped STA_2PbBr_4 perovskite only had a low PLQY of 2.79%, Mn doping was introduced to increase the Stokes shift and reduce the reabsorption, and the PLQY was boosted to 58.58% for Mn–STA_2PbBr_4. Fast neutron radioluminescence tests revealed the highest light yield (79% of that of a commercial reference ZnS(Ag):PP scintillator) for a Mn–STA_2PbBr_4 film with a thickness of 1135 μm. The spatial resolution was determined as 0.5 lp mm^{-1}, much higher than the previous reported value from perovskite NC solution,[118] but still lower than that of the industrial standard ZnS(Ag):PP (2 lp mm^{-1}). (Fig. 5g and h) This work opened new routes for fast neutron scintillators based on solid form perovskites. Further improvements need to focus on increasing the neutron scattering cross section to reduce the film thickness, improving the crystal quality to reduce light scattering and enhancing the light yield.

For fast neutron detection, scintillators have received much more attention than solid-state detectors owning to the easier

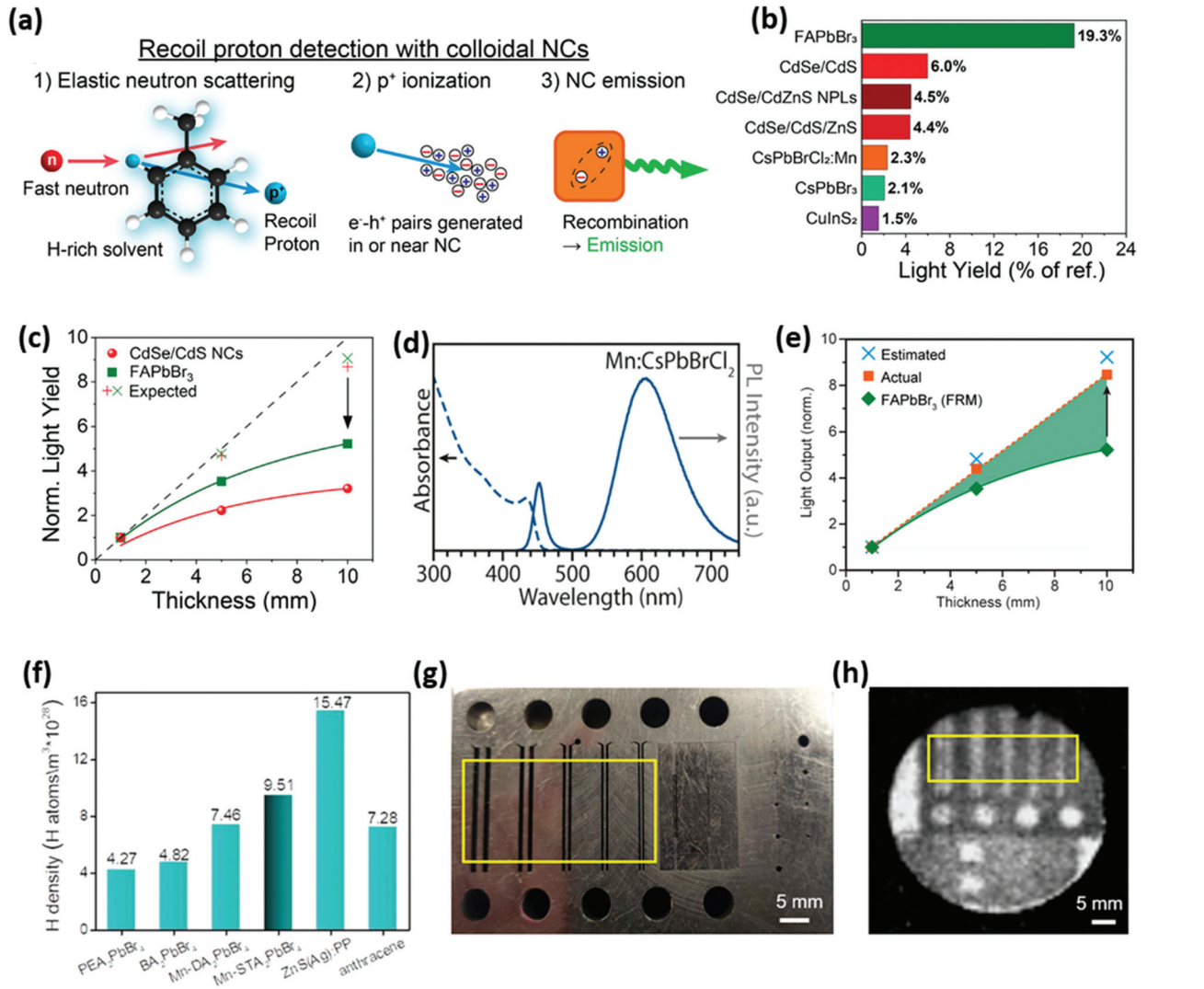

Fig. 5 (a) Sketch illustrating the principles of fast neutron detection: (1) elastic scattering of the fast neutron off an H nucleus; (2) the generation of a charge carrier cloud by the proton; (3) the excitation and emission of the NC. (b) Comparison of light yields obtained for different NCs under a 300 s fast neutron beam exposure, expressed as a percentage of the light yield obtained under identical conditions for the reference ZnS:Cu(PP) scintillator screen. (c) Normalized light yield *vs.* scintillator thickness for $FAPbBr_3$ and CdSe/CdS NCs at full concentration. The reduction of light yield compared with expected values was due to self-absorption. Reproduced with permission from ref. 118. Published 2020. Licenced under CC-BY-NC-ND 4.0. (d) Absorption and PL spectra of Mn doped $CsPbBrCl_2$ NCs. (e) Normalized light yield *vs.* scintillator thickness for 66% Mn^{2+}:$CsPbBrCl_2$ NCs (orange square) indicating a nearly linear response because of reduced reabsorption, in sharp contrast to the $FAPbBr_3$ NCs (green diamond). Reproduced with permission from ref. 69. Published 2021. Licenced under CC-BY-NC-ND 4.0. (f) Comparison of hydrogen density of a 2D perovskite and commercial fast neutron scintillators (ZnS(Ag):PP and anthracene). (g) Standard sample (steel plate with slits, holes of different sizes) for resolution test. (h) Fast neutron imaging proving good spatial resolution of the NC scintillator. The image was exposed for 100 s under a 14 MeV fast neutron accelerator for a total of 20 times. Reproduced with permission from ref. 70. Copyright 2021 American Chemical Society.

incorporation of hydrogen into the absorbing material, and perovskite scintillators have seen significant progress during the past few years. But the reported perovskite scintillators still have lower light yield and spatial resolution compared with commercial scintillators. Since the fundamental working principles of thermal and fast neutron scintillators are the same, that is perovskite single crystals or nanocrystals with high neutron capture cross section and high luminescence yield, future research needs to address these issues through the rational design of material composition, for example, exploring new halide perovskites with high density of H, ^{10}B or ^{6}Li and developing luminescence doping (Eu or Tl) in perovskites to improve light yield and reduce reabsorption.

5. Halide perovskites for photocathodes

Photocathodes are essential components in electron accelerators, for example, synchrotron light sources and free-electron

lasers. Photocathodes are also important parts in sensitive photodetectors, for example, PMTs and image intensifiers.[119–121] All of these applications rely on converting photons into photoelectrons by the photocathodes using photoelectric effect. The photoelectric effect, originally discovered more than 130 years ago, is the absorption of a photon with energy larger than a threshold value and emission of a photoelectron from the cathode. The threshold photon energy is defined as the work function of the cathode material, which equals to the energy difference between the Fermi level of the cathode and the vacuum level. Commonly used photocathode materials can be grouped into three categories: metals, positive electron affinity (PEA) semiconductors and negative electron affinity (NEA) semiconductors. Metals (Cu, Nb, Pb, Mg, *etc.*), benefiting from their low thermal emittance, high robustness, and long lifetime, are predominantly used in photoinjectors for accelerators.[122–126] However, their high work function and low photoemission quantum efficiency (QE) limit their further applications. Positive electron affinity semiconductors are mostly alkali compounds (Cs_3Sb, Na_2KSb, K_2CsSb, Cs_2Te, *etc.*). They have much lower work functions than metals. Therefore, they are widely used in photoinjectors requiring high current density and sensitive photodetectors for visible wavelength.[121,127] NEA semiconductors are typically III–V semiconductors (GaAs, GaN, tertiary alloys of III–V materials) with surface activated to NEA condition by a thin Cs (Cs–O or Cs–F) layer. The NEA surface greatly increases the electron escape probability, improves QE, and decreases thermal emittance.[128,129] They are also sensitive to visible or near infrared (NIR) wavelength, leading to the development of third-generation image intensifier.[130,131]

The semiconductors for NEA photocathodes need to meet a few requirements: high crystal quality for long carrier diffusion length, high optical absorption coefficient for efficient photoelectron generation, suitable optical bandgaps for high power lasers, and low surface defects for high electron emission probability. III–V semiconductors (GaAs, GaN) are the most widely used materials for NEA photocathode. However, high quality single crystals and rigorous surface preparations are required for the NEA activation,[132–134] and the lifetime of these NEA photocathodes is very limited due to the reactive surface Cs coating layer.[135]

Recently, Liu *et al.* demonstrated that inorganic perovskite ($CsPbBr_3$ and $CsPbI_3$) thin films can be used as efficient NEA photocathodes by deposition of a monolayer of Cs on their surfaces, summarized in Table 6.[136] The perovskite films were prepared by a simple spin-casting method, which can be applied for large scale production. Cs was thermally evaporated to activate the NEA surface state of perovskite films in ultra-high vacuum while simultaneously monitoring the photoemission QE until it reached the maximum value. Compared with the work function of pristine $CsPbBr_3$ and $CsPbI_3$ films measured by photoemission yield spectroscopy (4.0 eV), the work function of Cs-coated films was lowered to close to their optical band gaps of 2.1 eV and 1.8 eV, respectively. The maximum QE (2.2%) was achieved from $CsPbBr_3$ at an incident photon energy of 5 eV. (Fig. 6a and b) The lower QE from $CsPbI_3$ was attributed to the lower crystal quality due to the existence of non-perovskite yellow phase. Using Auger electron spectroscopy, the Cs coverage was quantitatively measured to be 2.5 atoms per unit cell of $CsPbBr_3$. The reproducibility of NEA perovskite photocathodes was further examined by testing seventeen $CsPbBr_3$ films, which gave an averaged QE of 1.5%. The perovskite photocathode also had improved stability compared to GaAs photocathodes as they underwent a slower degradation in similar vacuum conditions. In addition,

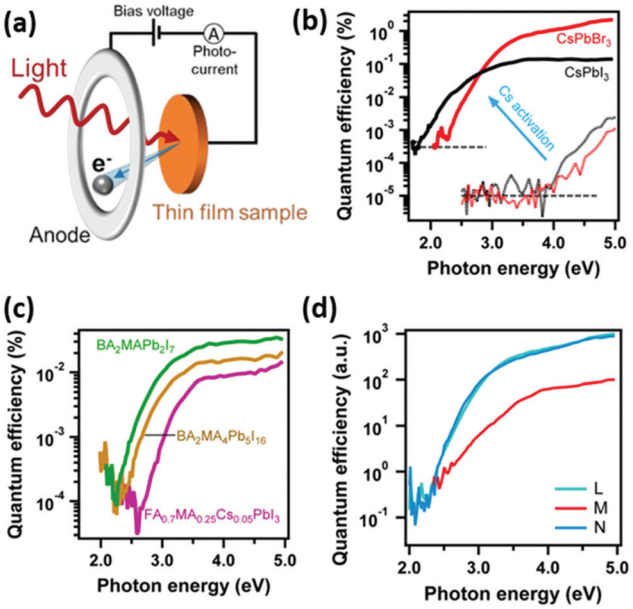

Fig. 6 (a) Sketch of the photoelectric effect measurement setup. The perovskite films were mounted inside an ultrahigh vacuum chamber. The bias voltage was applied between the perovskite cathode and a metal ring anode. (b) Quantum efficiency spectra of the photoelectric effect in the $CsPbI_3$ and $CsPbBr_3$ thin films before (dashed lines) and after (solid lines) Cs activation. Dashed grey horizontal lines indicate the emission threshold. (c) Quantum efficiency spectra of the photoelectric effect for the organic–inorganic perovskite films: $FA_{0.7}MA_{0.25}Cs_{0.05}PbI_3$, $BA_2MAPb_2I_7$, and $BA_2MA_4Pb_5I_{16}$. (d) Quantum efficiency spectra of an originally activated $CsPbBr_3$ photocathode (L), degraded photocathode (M), and reactivated photocathode (N). Reproduced with permission from ref. 136. Published 2021. Licensed under CC BY 4.0.

Table 6 Performance of perovskite photocathodes

Material	Growth method	Photoluminescence (nm)	Work function	Quantum efficiency (%)	Vacuum and lifetime	Ref.
Cs:$CsPbBr_3$ film	Spin coating	525	2.1	2.2	10^{-9} torr, 25 h	136
Cs:$CsPbI_3$ film	Spin coating	690	1.8	0.14	—	136

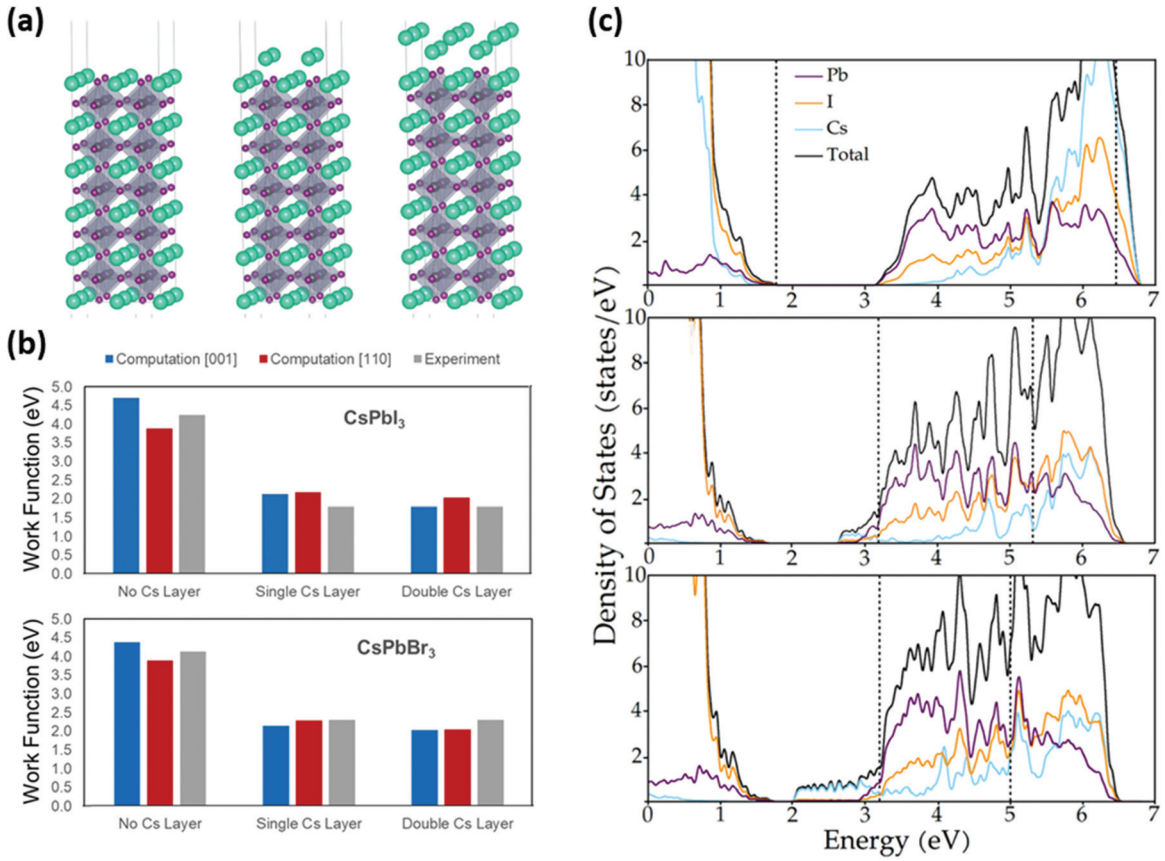

Fig. 7 (a) Model of the [001] surface slab of $CsPbX_3$ with no Cs coating (top), a single coating (middle), and a dense coating (bottom). (b) Calculated work function values of $CsPbI_3$ (top) and $CsPbBr_3$ (bottom) compared with experimental values. (c) Density of states (DOS) of $CsPbI_3$ for the [001] surface without Cs (top), with a single layer of Cs (middle), and with a double layer of Cs (bottom). Reproduced with permission from ref. 137. Copyright 2021 American Chemical Society.

degraded perovskite photocathodes can be regenerated by *in situ* Cs deposition (Fig. 6d).

A theoretical study of the origin of the reduced work function of Cs-coated halide perovskites was carried out by Lewis *et al.*[137] They used density functional theory (DFT) to investigate Cs-coated halide perovskites. A single-layer Cs coating can reduce the work function of $CsPbBr_3$ and $CsPbI_3$ [001] surfaces from ~4 eV to ~2.1 eV, and a double-layer Cs coating further lowered the work function to 2.0 eV and 1.8 eV, respectively. (Fig. 7a–c) These work functions and Cs coverage values matched the experimental results very well.[136] Traoré *et al.* studied the effects of surface dipoles on the work function of halide perovskites by combining classical electromagnetism and first-principle calculations and applied this theoretical methodology to various systems.[138] They found that a monolayer Cs coverage on $CsPbI_3$ can reduce the valence band energy level by 2.63 to 2.88 eV for different surface terminations (PbI_2 or CsI). These values were also consistent with previous reports.[136,137]

Beside inorganic perovskites, Liu *et al.* also tested organic–inorganic halide perovskites, including triple cation $FA_{0.7}MA_{0.25}Cs_{0.05}PbI_3$ and Ruddlesden-Popper layered perovskites ($BA_2MA_1Pb_2I_7$ and $BA_2MA_4Pb_5I_{16}$).[136] (Fig. 6c) After Cs activation, all three perovskites exhibited lowered photoemission onsets, but these values were still higher than their optical band gaps. Thus, the NEA status was not established on the organic–inorganic perovskites. These observations along with the relatively low QE from NEA $CsPbBr_3$ photocathode indicated the importance of reducing surface defects in order to fabricate high QE perovskite photocathodes.

Further developments of NEA perovskite photocathodes need to focus on improving the crystal quality, controlling the Cs activation process, and investigating the degradation mechanism. Although the inorganic perovskite photocathodes have much higher stability than III–V semiconductors, the QEs of the former are significantly lower than the latter. Therefore, high-quality perovskite crystals, especially single crystal thin films are the ideal materials for achieving high QE. The recent progress on the growth of high-quality single crystal perovskites through both Bridgman and solution methods provides new opportunities to improve the performance of perovskite photocathode.

6. Conclusions and outlooks

Halide perovskite detectors for particle radiation and photocathodes have seen a rapid development during the past five

years, especially for the detection of β particles and neutrons over the last two years. Compared with traditional detectors and photocathodes, the advantages of halide perovskites are the widely tunable compositions for meeting the various requirements of different types of radiation, versatile and low-cost synthesis for large-scale production, and superior electronic and optical properties for fast and efficient detection. Perovskite photocathodes and detectors for particle radiation, being still at the very early stage of developing, lag significantly behind traditional materials, *i.e.*, the energy resolutions of α, β and neutron detectors are far below those of state-of-the art technologies and the detection efficiencies are also much lower than those of established materials. Therefore, more efforts are needed to develop practical particle radiation detectors and photocathodes using halide perovskites.

Solid state perovskite detectors for α particles have been demonstrated for energy-resolved spectra, although their energy resolution still much lower than the best diamond-based detectors. In order to improve the detection efficiency and energy resolution, both material synthesis and device design need further development. Since the penetration depth of α particles is short, thin perovskite crystals with coplanar contacts may offer better detection performance. In case of the scintillators, perovskite nanocrystals are promising candidates since they may have better scintillation efficiency.

Halide perovskite detectors for β particles have only been shown as scintillators with two perovskites. Since the detection of β particles is very similar to that of X-/γ-ray which relies on the creation of secondary electrons, the perovskites that have been proved as efficient X-/γ-ray detectors may also be good detectors for β particles, providing the effect of electron back-scattering can be addressed.

Thermal neutron detectors based on halide perovskites are currently focused on indirect-conversion solid-state detectors, although they have realized reasonable detection efficiency, future research should focus on the direct-conversion detectors which have higher detection efficiency. On the other hand, perovskite detectors for fast neutrons are primarily scintillators for their high hydrogen concentration, especially in the form of colloidal nanocrystals. Both solid scintillators and solid-state detectors based on halide perovskites are underdeveloped and need more attention.

Photocathodes based on halide perovskite, being at early stage of development, have shown much improved stability than conventional semiconductors. The primary issue is their low QE. Therefore, future studies need to accomplish the growth of high-quality perovskite crystals with low surface defect density as well as discovering new perovskites that can work with infrared wavelength.

A comparable scenario is the evolution of perovskite γ-ray detectors, which were first reported in 2016 with an energy resolution of 35%.[56] After continuous development over the past few years, the best perovskite γ-ray detectors using $CsPbBr_3$ single crystals have been able to outperform the commercial CZT detectors with an energy resolution of 1.4%.[57] Hence, we are confident that advances in perovskite radiation detectors and photocathodes will create new opportunities also in the fields of particle radiation detection and photocathodes.

Conflicts of interest

There are no conflicts to declare.

Acknowledgements

This work is supported by the National Natural Science Foundation of China (22105018, 22179009, 22005034). F. L. acknowledges the support from Beijing Institute of Technology Research Fund Program for Young Scholars.

References

1 J. Eberth and J. Simpson, *Prog. Part. Nucl. Phys.*, 2008, **60**, 283–337.
2 P. D'Avanzo, *J. High Energy Astrophys.*, 2015, **7**, 73–80.
3 P. Delpierre, J. F. Berar, L. Blanquart, B. Caillot, J. C. Clemens and C. Mouget, *IEEE Trans. Nucl. Sci.*, 2001, **48**, 987–991.
4 L. Randaccio, S. Geremia, G. Nardin and J. Wuerges, *Coord. Chem. Rev.*, 2006, **250**, 1332–1350.
5 A. Marcelli, A. Cricenti, W. M. Kwiatek and C. Petibois, *Biotechnol. Adv.*, 2012, **30**, 1390–1404.
6 M. Hoheisel, *Nucl. Instrum. Methods Phys. Res., Sect. A*, 2006, **563**, 215–224.
7 R. Hanke, T. Fuchs and N. Uhlmann, *Nucl. Instrum. Methods Phys. Res., Sect. A*, 2008, **591**, 14–18.
8 K. Wells and D. A. Bradley, *Appl. Radiat. Isot.*, 2012, **70**, 1729–1746.
9 H. J. Wollersheim, D. E. Appelbe, A. Banu, R. Bassini, T. Beck, F. Becker, P. Bednarczyk, K. H. Behr, M. A. Bentley, G. Benzoni, C. Boiano, U. Bonnes, A. Bracco, S. Brambilla, A. Brünle, A. Bürger, K. Burkard, P. A. Butler, F. Camera, D. Curien, J. Devin, P. Doornenbal, C. Fahlander, K. Fayz, H. Geissel, J. Gerl, M. Górska, H. Grawe, J. Grebosz, R. Griffiths, G. Hammond, M. Hellström, J. Hoffmann, H. Hübel, J. Jolie, J. V. Kalben, M. Kmiecik, I. Kojouharov, R. Kulessa, N. Kurz, I. Lazarus, J. Li, J. Leske, R. Lozeva, A. Maj, S. Mandal, W. Męczyński, B. Million, G. Münzenberg, S. Muralithar, M. Mutterer, P. J. Nolan, G. Neyens, J. Nyberg, W. Prokopowicz, V. F. E. Pucknell, P. Reiter, D. Rudolph, N. Saito, T. R. Saito, D. Seddon, H. Schaffner, J. Simpson, K. H. Speidel, J. Styczeń, K. Sümmerer, N. Warr, H. Weick, C. Wheldon, O. Wieland, M. Winkler and M. Zięblíński, *Nucl. Instrum. Methods Phys. Res., Sect. A*, 2005, **537**, 637–657.
10 D. C. Kocher, *Nucl. Sci. Eng.*, 1982, **82**, 477.

11 R. Rieder, R. Gellert, J. Brückner, G. Klingelhöfer, G. Dreibus, A. Yen and S. W. Squyres, *J. Geophys. Res.: Planets*, 2003, **108**, 8066.
12 G. R. Gilmore, *Practical Gamma–Ray Spectrometry*, 2008, ch. 2, pp. 25–38.
13 A. Owens and A. Peacock, *Nucl. Instrum. Methods Phys. Res., Sect. A*, 2004, **531**, 18–37.
14 C. W. E. van Eijk, *Nucl. Instrum. Methods Phys. Res., Sect. A*, 2001, **460**, 1–14.
15 E. Rutherford, *Lond. Edinb. Dublin philos. Mag. J. Sci.*, 1911, **21**, 669–688.
16 C. F. Williamson, J. Boujot and J. Picard, *Tables of Range and Stopping Power of Chemical Elements for Charged Particles of Energy 0.5 to 500 MeV*, France, 1966.
17 V. Lazurik, V. Moskvin and T. Tabata, *IEEE Trans. Nucl. Sci.*, 1998, **45**, 626–631.
18 R. Hippler, K. Saeed, I. McGregor and H. Kleinpoppen, *Phys. Rev. Lett.*, 1981, **46**, 1622–1625.
19 V. F. Sears, *Thermal-neutron scattering lengths and cross sections for condensed-matter research*, Canada, 1984.
20 B. D. Milbrath, A. J. Peurrung, M. Bliss and W. J. Weber, *J. Mater. Res.*, 2011, **23**, 2561–2581.
21 N. Kardjilov, I. Manke, A. Hilger, M. Strobl and J. Banhart, *Mater. Today*, 2011, **14**, 248–256.
22 S. O. Kasap, *J. Phys. D: Appl. Phys.*, 2000, **33**, 2853–2865.
23 I. Y. Lee, M. A. Deleplanque and K. Vetter, *Rep. Prog. Phys.*, 2003, **66**, 1095–1144.
24 S. Watanabe, S. N. Ishikawa, H. Aono, S. Takeda, H. Odaka, M. Kokubun, T. Takahashi, K. Nakazawa, H. Tajima, M. Onishi and Y. Kuroda, *IEEE Trans. Nucl. Sci.*, 2009, **56**, 777–782.
25 K. Saito, I. Tanihata, M. Fujiwara, T. Saito, S. Shimoura, T. Otsuka, Y. Onda, M. Hoshi, Y. Ikeuchi, F. Takahashi, N. Kinouchi, J. Saegusa, A. Seki, H. Takemiya and T. Shibata, *J. Environ. Radioact.*, 2015, **139**, 308–319.
26 P. J. Sellin, *Nucl. Instrum. Methods Phys. Res., Sect. A*, 2003, **513**, 332–339.
27 E. Fredenberg, *Nucl. Instrum. Methods Phys. Res., Sect. A*, 2018, **878**, 74–87.
28 R. Caciuffo, G. Amoretti, A. Murani, R. Sessoli, A. Caneschi and D. Gatteschi, *Phys. Rev. Lett.*, 1998, **81**, 4744–4747.
29 S. Siegel, R. W. Silverman, S. Yiping and S. R. Cherry, *IEEE Trans. Nucl. Sci.*, 1996, **43**, 1634–1641.
30 K. S. Shah, J. Glodo, M. Klugerman, W. M. Higgins, T. Gupta and P. Wong, *IEEE Trans. Nucl. Sci.*, 2004, **51**, 2395–2399.
31 W. Becker, A. Bergmann and C. Biskup, *Microsc. Res. Tech.*, 2007, **70**, 403–409.
32 M. J. Sanderson, I. Smith, I. Parker and M. D. Bootman, *Cold Spring Harbor protocols*, 2014, pp. 1042–1065.
33 A. K. Jena, A. Kulkarni and T. Miyasaka, *Chem. Rev.*, 2019, **119**, 3036–3103.
34 N.-G. Park, *Mater. Today*, 2015, **18**, 65–72.
35 C. C. Stoumpos, D. H. Cao, D. J. Clark, J. Young, J. M. Rondinelli, J. I. Jang, J. T. Hupp and M. G. Kanatzidis, *Chem. Mater.*, 2016, **28**, 2852–2867.
36 J. Yin, P. Maity, M. De Bastiani, I. Dursun, O. M. Bakr, J.-L. Brédas and O. F. Mohammed, *Sci. Adv.*, 2017, **3**, e1701793.
37 L. Schade, A. D. Wright, R. D. Johnson, M. Dollmann, B. Wenger, P. K. Nayak, D. Prabhakaran, L. M. Herz, R. Nicholas, H. J. Snaith and P. G. Radaelli, *ACS Energy Lett.*, 2019, **4**, 299–305.
38 R. Zhuang, X. Wang, W. Ma, Y. Wu, X. Chen, L. Tang, H. Zhu, J. Liu, L. Wu, W. Zhou, X. Liu and Y. Yang, *Nat. Photonics*, 2019, **13**, 602–608.
39 J.-P. Correa-Baena, M. Saliba, T. Buonassisi, M. Grätzel, A. Abate, W. Tress and A. Hagfeldt, *Science*, 2017, **358**, 739.
40 H. Tsai, R. Asadpour, J.-C. Blancon, C. C. Stoumpos, O. Durand, J. W. Strzalka, B. Chen, R. Verduzco, P. M. Ajayan, S. Tretiak, J. Even, M. A. Alam, M. G. Kanatzidis, W. Nie and A. D. Mohite, *Science*, 2018, **360**, 67.
41 Y. Wang, Z. Zhang, M. Tao, Y. Lan, M. Li, Y. Tian and Y. Song, *Nanoscale*, 2020, **12**, 18563–18575.
42 X.-K. Liu, W. Xu, S. Bai, Y. Jin, J. Wang, R. H. Friend and F. Gao, *Nat. Mater.*, 2021, **20**, 10–21.
43 H. Tsai, W. Nie, J.-C. Blancon, C. C. Stoumpos, C. M. M. Soe, J. Yoo, J. Crochet, S. Tretiak, J. Even, A. Sadhanala, G. Azzellino, R. Brenes, P. M. Ajayan, V. Bulović, S. D. Stranks, R. H. Friend, M. G. Kanatzidis and A. D. Mohite, *Adv. Mater.*, 2018, **30**, 1704217.
44 Y. Guo, F. Gao, P. Huang, R. Wu, W. Gu, J. Wei, F. Liu and H. Li, *Energy Mater. Adv.*, 2022, **2022**, 9857943.
45 J. C. Yu, J. H. Park, S. Y. Lee and M. H. Song, *Nanoscale*, 2019, **11**, 1505–1514.
46 H. Dong, C. Zhang, X. Liu, J. Yao and Y. S. Zhao, *Chem. Soc. Rev.*, 2020, **49**, 951–982.
47 H. Wang and D. H. Kim, *Chem. Soc. Rev.*, 2017, **46**, 5204–5236.
48 F. Paulus, C. Tyznik, O. D. Jurchescu and Y. Vaynzof, *Adv. Funct. Mater.*, 2021, **31**, 2101029.
49 N. D. Canicoba, N. Zagni, F. Liu, G. McCuistian, K. Fernando, H. Bellezza, B. Traoré, R. Rogel, H. Tsai, L. Le Brizoual, W. Nie, J. J. Crochet, S. Tretiak, C. Katan, J. Even, M. G. Kanatzidis, B. W. Alphenaar, J.-C. Blancon, M. A. Alam and A. D. Mohite, *ACS Mater. Lett.*, 2019, **1**, 633–640.
50 G. Zhang, G. Liu, L. Wang and J. T. S. Irvine, *Chem. Soc. Rev.*, 2016, **45**, 5951–5984.
51 Y. Zhou, J. Chen, O. M. Bakr and O. F. Mohammed, *ACS Energy Lett.*, 2021, **6**, 739–768.
52 Y. C. Kim, K. H. Kim, D. Y. Son, D. N. Jeong, J. Y. Seo, Y. S. Choi, I. T. Han, S. Y. Lee and N. G. Park, *Nature*, 2017, **550**, 87–91.
53 M. Gandini, I. Villa, M. Beretta, C. Gotti, M. Imran, F. Carulli, E. Fantuzzi, M. Sassi, M. Zaffalon, C. Brofferio, L. Manna, L. Beverina, A. Vedda, M. Fasoli, L. Gironi and S. Brovelli, *Nat. Nanotechnol.*, 2020, **15**, 462–468.
54 H. Tsai, F. Liu, S. Shrestha, K. Fernando, S. Tretiak, B. Scott, D. T. Vo, J. Strzalka and W. Nie, *Sci. Adv.*, 2020, **6**, eaay0815.

55 C. Rodà, M. Fasoli, M. L. Zaffalon, F. Cova, V. Pinchetti, J. Shamsi, A. L. Abdelhady, M. Imran, F. Meinardi, L. Manna, A. Vedda and S. Brovelli, *Adv. Funct. Mater.*, 2021, **31**, 2104879.
56 S. Yakunin, D. N. Dirin, Y. Shynkarenko, V. Morad, I. Cherniukh, O. Nazarenko, D. Kreil, T. Nauser and M. V. Kovalenko, *Nat. Photonics*, 2016, **10**, 585–589.
57 Y. He, M. Petryk, Z. Liu, D. G. Chica, I. Hadar, C. Leak, W. Ke, I. Spanopoulos, W. Lin, D. Y. Chung, B. W. Wessels, Z. He and M. G. Kanatzidis, *Nat. Photonics*, 2021, **15**, 35–42.
58 F. Liu, M. Yoho, H. Tsai, K. Fernando, J. Tisdale, S. Shrestha, J. K. Baldwin, A. D. Mohite, S. Tretiak, D. T. Vo and W. Nie, *Mater. Today*, 2020, **37**, 27–34.
59 F. Liu, R. Wu, J. Wei, W. Nie, A. D. Mohite, S. Brovelli, L. Manna and H. Li, *ACS Energy Lett.*, 2022, 1066–1085, DOI: **10.1021/acsenergylett.2c00031**.
60 Z. Li, F. Zhou, H. Yao, Z. Ci, Z. Yang and Z. Jin, *Mater. Today*, 2021, **48**, 155–175.
61 Y. He, I. Hadar and M. G. Kanatzidis, *Nat. Photonics*, 2022, **16**, 14–26.
62 H. Wei and J. Huang, *Nat. Commun.*, 2019, **10**, 1066.
63 Q. Xu, H. Wei, W. Wei, W. Chuirazzi, D. DeSantis, J. Huang and L. Cao, *Nucl. Instrum. Methods Phys. Res., Sect. A*, 2017, **848**, 106–108.
64 K. M. McCall, Z. Liu, G. Trimarchi, C. C. Stoumpos, W. Lin, Y. He, I. Hadar, M. G. Kanatzidis and B. W. Wessels, *ACS Photonics*, 2018, **5**, 3748–3762.
65 B. Xiao, Q. Sun, S. Wang, L. Ji, Y. Li, S. Xi, B.-B. Zhang, J. Wang, W. Jie and Y. Xu, *J. Phys. Chem. Lett.*, 2022, 1187–1193, DOI: **10.1021/acs.jpclett.1c04204**.
66 D. Yu, P. Wang, F. Cao, Y. Gu, J. Liu, Z. Han, B. Huang, Y. Zou, X. Xu and H. Zeng, *Nat. Commun.*, 2020, **11**, 3395.
67 L. Fernandez-Izquierdo, M. G. Reyes-Banda, X. Mathew, I. R. Chavez-Urbiola, L. El Bouanani, J. Chang, C. Avila-Avendano, N. R. Mathews, M. I. Pintor-Monroy and M. Quevedo-Lopez, *Adv. Mater. Technol.*, 2020, **5**, 2000534.
68 A. Xie, C. Hettiarachchi, F. Maddalena, M. E. Witkowski, M. Makowski, W. Drozdowski, A. Arramel, A. T. S. Wee, S. V. Springham, P. Q. Vuong, H. J. Kim, C. Dujardin, P. Coquet, M. D. Birowosuto and C. Dang, *Commun. Mater.*, 2020, **1**, 37.
69 F. Montanarella, K. M. McCall, K. Sakhatskyi, S. Yakunin, P. Trtik, C. Bernasconi, I. Cherniukh, D. Mannes, M. I. Bodnarchuk, M. Strobl, B. Walfort and M. V. Kovalenko, *ACS Energy Lett.*, 2021, **6**, 4365–4373.
70 J. Zheng, Y. Zeng, J. Wang, C. Sun, B. Tang, Y. Wu, Y. Zhang, Y. Yi, N. Wang, Y. Zhao and S. Zhou, *J. Am. Chem. Soc.*, 2021, **143**, 21302–21311.
71 Y. He, W. Ke, G. C. B. Alexander, K. M. McCall, D. G. Chica, Z. Liu, I. Hadar, C. C. Stoumpos, B. W. Wessels and M. G. Kanatzidis, *ACS Photonics*, 2018, **5**, 4132–4138.
72 Y. Li, W. Shao, L. Chen, J. Wang, J. Nie, H. Zhang, S. Zhang, R. Gao, X. Ouyang, X. Ouyang and Q. Xu, *NPG Asia Mater.*, 2021, **13**, 40.
73 G. Jia and J. Jia, *J. Environ. Radioact.*, 2012, **106**, 98–119.
74 T. Shimaoka, J. H. Kaneko, Y. Sato, M. Tsubota, H. Shimmyo, A. Chayahara, H. Watanabe, H. Umezawa and Y. Mokuno, *Phys. Status Solidi A*, 2016, **213**, 2629–2633.
75 T. Shimaoka, J. H. Kaneko, M. Tsubota, H. Shimmyo, H. Watanabe, A. Chayahara, H. Umezawa and S.-i. Shikata, *EPL*, 2016, **113**, 62001.
76 S. Jagtap, P. Chopade, S. Tadepalli, A. Bhalerao and S. Gosavi, *Opto-Electron. Rev.*, 2019, **27**, 90–103.
77 W. G. Lee, Y. K. Kim, J. K. Kim, H. J. Seo, V. Ryzhikov, N. Starzhinskiy, O. Vyagin, K. Katrunov and O. Zelenskaya, *J. Korean Phys. Soc.*, 2006, **48**, 47–50.
78 Y. He, Z. Liu, K. M. McCall, W. Lin, D. Y. Chung, B. W. Wessels and M. G. Kanatzidis, *Nucl. Instrum. Methods Phys. Res., Sect. A*, 2019, **922**, 217–221.
79 Y. Li, L. Chen, B. Liu, P. Jin, R. Gao, L. Zhou, P. Wan, Q. Xu and X. Ouyang, *J. Mater. Chem. C*, 2021, **9**, 17124–17128.
80 Y. Li, L. Chen, R. Gao, B. Liu, W. Zheng, Y. Zhu, J. Ruan, X. Ouyang and Q. Xu, *ACS Appl. Mater. Interfaces*, 2022, **14**, 1489–1495.
81 P. Zhao, J. Su, Y. Guo, L. Wang, Z. Lin, Y. Hao, X. Ouyang and J. Chang, *Nano Res.*, 2022, **15**, 2697–2705.
82 P. Zhao, J. Su, Y. Guo, L. Wang, Z. Lin, J. Zhang, Y. Hao, X. Ouyang and J. Chang, *Mater. Today Phys.*, 2021, **20**, 100446.
83 C. C. Stoumpos, C. D. Malliakas, J. A. Peters, Z. Liu, M. Sebastian, J. Im, T. C. Chasapis, A. C. Wibowo, D. Y. Chung, A. J. Freeman, B. W. Wessels and M. G. Kanatzidis, *Cryst. Growth Des.*, 2013, **13**, 2722–2727.
84 D. H. Cao, C. C. Stoumpos, O. K. Farha, J. T. Hupp and M. G. Kanatzidis, *J. Am. Chem. Soc.*, 2015, **137**, 7843–7850.
85 C. C. Stoumpos, C. M. M. Soe, H. Tsai, W. Nie, J.-C. Blancon, D. H. Cao, F. Liu, B. Traoré, C. Katan, J. Even, A. D. Mohite and M. G. Kanatzidis, *Chem*, 2017, **2**, 427–440.
86 J.-C. Blancon, J. Even, C. C. Stoumpos, M. G. Kanatzidis and A. D. Mohite, *Nat. Nanotechnol.*, 2020, **15**, 969–985.
87 M. I. Saidaminov, J. Almutlaq, S. Sarmah, I. Dursun, A. A. Zhumekenov, R. Begum, J. Pan, N. Cho, O. F. Mohammed and O. M. Bakr, *ACS Energy Lett.*, 2016, **1**, 840–845.
88 A. Ray, D. Maggioni, D. Baranov, Z. Dang, M. Prato, Q. A. Akkerman, L. Goldoni, E. Caneva, L. Manna and A. L. Abdelhady, *Chem. Mater.*, 2019, **31**, 7761–7769.
89 U. Petralanda, G. Biffi, S. C. Boehme, D. Baranov, R. Krahne, L. Manna and I. Infante, *Nano Lett.*, 2021, **21**, 8619–8626.
90 L. Wang, H. Liu, Y. Zhang and O. F. Mohammed, *ACS Energy Lett.*, 2020, **5**, 87–99.
91 Q. Chen, J. Wu, X. Ou, B. Huang, J. Almutlaq, A. A. Zhumekenov, X. Guan, S. Han, L. Liang, Z. Yi, J. Li, X. Xie, Y. Wang, Y. Li, D. Fan, D. B. L. Teh, A. H. All, O. F. Mohammed, O. M. Bakr, T. Wu, M. Bettinelli, H. Yang, W. Huang and X. Liu, *Nature*, 2018, **561**, 88–93.

92 B.-B. Zhang, F. Wang, X. Liu, B. Xiao, M. Xu, S.-T. Dong, Y. Xu, P. Sellin and W. Jie, *J. Phys. Chem. C*, 2021, **125**, 4235–4242.
93 F. O. Ogundare and O. I. Adekoya, *J. Radiat. Res. Appl. Sci.*, 2015, **8**, 411–417.
94 T. Tabata, R. Ito and S. Okabe, *Nucl. Instrum. Methods*, 1971, **94**, 509–513.
95 L. N. Quan, M. Yuan, R. Comin, O. Voznyy, E. M. Beauregard, S. Hoogland, A. Buin, A. R. Kirmani, K. Zhao, A. Amassian, D. H. Kim and E. H. Sargent, *J. Am. Chem. Soc.*, 2016, **138**, 2649–2655.
96 H. Kang, S. Min, B. Seo, C. Roh, S. Hong and J. H. Cheong, *Chemosensors*, 2021, **9**, 53.
97 M. P. Blakeley, P. Langan, N. Niimura and A. Podjarny, *Curr. Opin. Struct. Biol.*, 2008, **18**, 593–600.
98 P. Filliatre, C. Jammes, B. Geslot and L. Buiron, *Ann. Nucl. Energy*, 2010, **37**, 1435–1442.
99 R. T. Kouzes, E. R. Siciliano, J. H. Ely, P. E. Keller and R. J. McConn, *Nucl. Instrum. Methods Phys. Res., Sect. A*, 2008, **584**, 383–400.
100 H. Tsuchiya, Y. Muraki, K. Masuda, Y. Matsubara, T. Koi, T. Sako, S. Ohno, T. Hoshida, S. Shibata, Y. Munakata, K. Hatanaka, T. Wakasa and H. Sakai, *Nucl. Instrum. Methods Phys. Res., Sect. A*, 2001, **463**, 183–193.
101 J. J. Valiente-Dobón, G. Jaworski, A. Goasduff, F. J. Egea, V. Modamio, T. Hüyük, A. Triossi, M. Jastrząb, P. A. Söderström, A. Di Nitto, G. de Angelis, G. de France, N. Erduran, A. Gadea, M. Moszyński, J. Nyberg, M. Palacz, R. Wadsworth, R. Aliaga, C. Aufranc, M. Bézard, G. Baulieu, E. Bissiato, A. Boujrad, I. Burrows, S. Carturan, P. Cocconi, G. Colucci, D. Conventi, M. Cordwell, S. Coudert, J. M. Deltoro, L. Ducroux, T. Dupasquier, S. Ertürk, X. Fabian, V. González, A. Grant, K. Hadyńska-Klęk, A. Illana, M. L. Jurado-Gomez, M. Kogimtzis, I. Lazarus, L. Legeard, J. Ljungvall, G. Pasqualato, R. M. Pérez-Vidal, A. Raggio, D. Ralet, N. Redon, F. Saillant, B. Sayğı, E. Sanchis, M. Scarcioffolo, M. Siciliano, D. Testov, O. Stezowski, M. Tripon and I. Zanon, *Nucl. Instrum. Methods Phys. Res., Sect. A*, 2019, **927**, 81–86.
102 I. Obodovskiy, *Radiation*, ed. I. Obodovskiy, Elsevier, 2019, pp. 151–160.
103 R. Zboray, R. Adams, M. Morgano and Z. Kis, *Nucl. Instrum. Methods Phys. Res., Sect. A*, 2019, **930**, 142–150.
104 A. N. Caruso, *J. Phys.: Condens. Matter*, 2010, **22**, 443201.
105 G. H. V. Bertrand, M. Hamel, S. Normand and F. Sguerra, *Nucl. Instrum. Methods Phys. Res., Sect. A*, 2015, **776**, 114–128.
106 J. A. Caraveo-Frescas, M. G. Reyes-Banda, L. Fernandez-Izquierdo and M. A. Quevedo-Lopez, *Adv. Mater. Technol.*, 2022, 2100956.
107 R. T. Kouzes, J. H. Ely, L. E. Erikson, W. J. Kernan, A. T. Lintereur, E. R. Siciliano, D. L. Stephens, D. C. Stromswold, R. M. Van Ginhoven and M. L. Woodring, *Nucl. Instrum. Methods Phys. Res., Sect. A*, 2010, **623**, 1035–1045.
108 C. W. E. van Eijk, A. Bessière and P. Dorenbos, *Nucl. Instrum. Methods Phys. Res., Sect. A*, 2004, **529**, 260–267.
109 R. J. Nikolić, C. L. Cheung, C. E. Reinhardt, T. F. Wang, *Proc. SPIE 6013, Optoelectronic Devices: Physics, Fabrication, and Application II*, 2005, 601305.
110 Q. Shao, L. F. Voss, A. M. Conway, R. J. Nikolic, M. A. Dar and C. L. Cheung, *Appl. Phys. Lett.*, 2013, **102**, 063505.
111 S. L. Bellinger, R. G. Fronk, W. J. McNeil, T. J. Sobering and D. S. McGregor, *IEEE Trans. Nucl. Sci.*, 2012, **59**, 167–173.
112 J. Li, R. Dahal, S. Majety, J. Y. Lin and H. X. Jiang, *Nucl. Instrum. Methods Phys. Res., Sect. A*, 2011, **654**, 417–420.
113 E. Tupitsyn, P. Bhattacharya, E. Rowe, L. Matei, M. Groza, B. Wiggins, A. Burger and A. Stowe, *Appl. Phys. Lett.*, 2012, **101**, 202101.
114 D. G. Chica, Y. He, K. M. McCall, D. Y. Chung, R. O. Pak, G. Trimarchi, Z. Liu, P. M. De Lurgio, B. W. Wessels and M. G. Kanatzidis, *Nature*, 2020, **577**, 346–349.
115 P. Andričević, G. Náfrádi, M. Kollár, B. Náfrádi, S. Lilley, C. Kinane, P. Frajtag, A. Sienkiewicz, A. Pautz, E. Horváth and L. Forró, *Sci. Rep.*, 2021, **11**, 17159.
116 L. El Bouanani, S. E. Keating, C. Avila-Avendano, M. G. Reyes-Banda, M. I. Pintor-Monroy, V. Singh, B. L. Murillo, M. Higgins and M. A. Quevedo-Lopez, *ACS Appl. Mater. Interfaces*, 2021, **13**, 28049–28056.
117 J. Dumazert, R. Coulon, Q. Lecomte, G. H. V. Bertrand and M. Hamel, *Nucl. Instrum. Methods Phys. Res., Sect. A*, 2018, **882**, 53–68.
118 K. M. McCall, K. Sakhatskyi, E. Lehmann, B. Walfort, A. S. Losko, F. Montanarella, M. I. Bodnarchuk, F. Krieg, Y. Kelestemur, D. Mannes, Y. Shynkarenko, S. Yakunin and M. V. Kovalenko, *ACS Nano*, 2020, **14**, 14686–14697.
119 S. H. Kong, J. Kinross-Wright, D. C. Nguyen and R. L. Sheffield, *Nucl. Instrum. Methods Phys. Res., Sect. A*, 1995, **358**, 272–275.
120 T. H. P. Chang, M. Mankos, K. Y. Lee and L. P. Muray, *Microelectron. Eng.*, 2001, **57–58**, 117–135.
121 K. Nakamura, Y. Hamana, Y. Ishigami and T. Matsui, *Nucl. Instrum. Methods Phys. Res., Sect. A*, 2010, **623**, 276–278.
122 W. S. Graves, L. F. DiMauro, R. Heese, E. D. Johnson, J. Rose, J. Rudati, T. Shaftan, B. Sheehy, *PACS2001. Proceedings of the 2001 Particle Accelerator Conference* (Cat. No.01CH37268), 2001, 2227–2229.
123 R. B. Cairns and J. A. R. Samson, *J. Opt. Soc. Am.*, 1966, **56**, 1568–1573.
124 D. H. Dowell, I. Bazarov, B. Dunham, K. Harkay, C. Hernandez-Garcia, R. Legg, H. Padmore, T. Rao, J. Smedley and W. Wan, *Nucl. Instrum. Methods Phys. Res., Sect. A*, 2010, **622**, 685–697.
125 T. Nakajyo, J. Yang, F. Sakai and Y. Aoki, *Jpn. J. Appl. Phys.*, 2003, **42**, 1470–1474.
126 J. Smedley, T. Rao and J. Sekutowicz, *Phys. Rev. Spec. Top. Accel Beams*, 2008, **11**, 013502.
127 D. H. Dowell, K. J. Davis, K. D. Friddell, E. L. Tyson, C. A. Lancaster, L. Milliman, R. E. Rodenburg, T. Aas, M. Bemes, S. Z. Bethel, P. E. Johnson, K. Murphy,

C. Whelen, G. E. Busch and D. K. Remelius, *Appl. Phys. Lett.*, 1993, **63**, 2035–2037.

128 I. V. Bazarov, B. M. Dunham, Y. Li, X. Liu, D. G. Ouzounov, C. K. Sinclair, F. Hannon and T. Miyajima, *J. Appl. Phys.*, 2008, **103**, 054901.

129 N. Yamamoto, M. Yamamoto, M. Kuwahara, R. Sakai, T. Morino, K. Tamagaki, A. Mano, A. Utsu, S. Okumi, T. Nakanishi, M. Kuriki, C. Bo, T. Ujihara and Y. Takeda, *J. Appl. Phys.*, 2007, **102**, 024904.

130 S. E. William, S. Richard, R. Larry, A. Avraham, *Proc. SPIE 1655, Electron Tubes and Image Intensifiers*, 1992, DOI: **10.1117/1112.60337**.

131 A. C. Kenneth, W. A. Verle, M. Hugh, *Proc. SPIE 1243, Electron Image Tubes and Image Intensifiers*, 1990, DOI: **10.1117/1112.19469**.

132 S. Pastuszka, M. Hoppe, D. Kratzmann, D. Schwalm, A. Wolf, A. S. Jaroshevich, S. N. Kosolobov, D. A. Orlov and A. S. Terekhov, *J. Appl. Phys.*, 2000, **88**, 6788–6800.

133 V. S. Khoroshilov, D. M. Kazantsev and A. G. Zhuravlev, *J. Phys. Conf. Ser.*, 2019, **1410**, 012128.

134 O. Siegmund, J. Vallerga, J. McPhate, J. Malloy, A. Tremsin, A. Martin, M. Ulmer and B. Wessels, *Nucl. Instrum. Methods Phys. Res., Sect. A*, 2006, **567**, 89–92.

135 N. Chanlek, J. D. Herbert, R. M. Jones, L. B. Jones, K. J. Middleman and B. L. Militsyn, *J. Phys. D: Appl. Phys.*, 2014, **47**, 055110.

136 F. Liu, S. Sidhik, M. A. Hoffbauer, S. Lewis, A. J. Neukirch, V. Pavlenko, H. Tsai, W. Nie, J. Even, S. Tretiak, P. M. Ajayan, M. G. Kanatzidis, J. J. Crochet, N. A. Moody, J.-C. Blancon and A. D. Mohite, *Nat. Commun.*, 2021, **12**, 673.

137 S. G. Lewis, D. Ghosh, K. L. Jensen, D. Finkenstadt, A. Shabaev, S. G. Lambrakos, F. Liu, W. Nie, J.-C. Blancon, L. Zhou, J. J. Crochet, N. Moody, A. D. Mohite, S. Tretiak and A. J. Neukirch, *J. Phys. Chem. Lett.*, 2021, **12**, 6269–6276.

138 B. Traoré, P. Basera, A. J. Ramadan, H. J. Snaith, C. Katan and J. Even, *ACS Energy Lett.*, 2022, **7**, 349–357.

